

BokehDepth: Enhancing Monocular Depth Estimation through Bokeh Generation

Hangwei Zhang^{1,2}, Armando Teles Fortes¹, Tianyi Wei¹, Xingang Pan^{1*}

¹S-Lab, Nanyang Technological University ²Beihang University

Project Page: https://fogradio.github.io/BokehDepth_Project/



Figure 1. *BokehDepth* decouples bokeh synthesis from depth prediction and uses lens-aware defocus as a supervision-free geometric cue to improve the accuracy and physical consistency of monocular depth estimation. *Left*: conventional pipelines predict depth from a single sharp image and render bokeh from the noisy depth map. *Right*: our two-stage framework, where Stage-1 generates a calibrated bokeh stack from a single image and Stage-2 built on UniDepthV2 [74] fuses defocus cues to produce sharper and more reliable metric depth.

Abstract

*Bokeh and monocular depth estimation are tightly coupled through the same lens imaging geometry, yet current methods exploit this connection in incomplete ways. High-quality bokeh rendering pipelines typically depend on noisy depth maps, which amplify estimation errors into visible artifacts, while modern monocular metric depth models still struggle on weakly textured, distant and geometrically ambiguous regions where defocus cues are most informative. We introduce **BokehDepth**, a two-stage framework that decouples bokeh synthesis from depth prediction and treats defocus as an auxiliary supervision-free geometric cue. In Stage-1, a physically guided controllable bokeh generator, built on a powerful pretrained image editing backbone, produces depth-free bokeh stacks with calibrated bokeh strength from a single sharp input. In Stage-2, a lightweight defocus-aware aggregation module plugs into*

existing monocular depth encoders, fuses features along the defocus dimension, and exposes stable depth-sensitive variations while leaving downstream decoder unchanged. Across challenging benchmarks, BokehDepth improves visual fidelity over depth-map-based bokeh baselines and consistently boosts the metric accuracy and robustness of strong monocular depth foundation models.

1. Introduction

Bokeh is a lens-originated optical effect that describes the aesthetic quality of out-of-focus regions, which often helps emphasize in-focus subjects by softly blurring distracting details [25, 58, 88]. Monocular depth estimation aims to predict the depth of each pixel relative to the camera from a single RGB image to recover the scene’s 3D geometry [19, 80, 84]. Monocular depth estimation and bokeh synthesis are intrinsically linked by the lens imag-

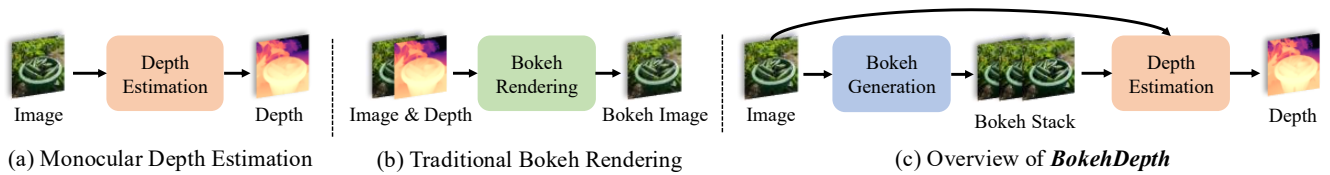


Figure 2. From monocular depth and depth-based bokeh to *BokehDepth*. (a) Standard monocular depth estimation predicts a depth map from a single RGB image. (b) Classical bokeh rendering takes an image and its depth map as input to synthesize bokeh. (c) *BokehDepth* first generates a calibrated bokeh stack from the input image, and then uses the induced defocus cues to enhance depth estimation.

ing geometry [68, 95]. Accurate depth maps enable physically consistent and controllable bokeh rendering [57, 89], and defocus cues from bokeh supply informative signals that help resolve geometric ambiguities in depth prediction [39, 97, 107].

Most high-quality bokeh rendering pipelines still rely on a depth or disparity map to guide spatially varying blur [58, 65, 66, 89, 124]. This requirement increases system complexity and makes the final visual quality tightly bounded by the depth estimator [25, 88]. Any local depth error is immediately translated into an incorrect blur radius or a broken occlusion edge [124]. Classical depth-from-defocus methods rely on multi-aperture pairs that are hard to acquire and their models often lack robustness across cameras and scenes [12, 23, 24, 39, 61, 97, 106]. Modern Monocular Metric Depth Estimation (MMDE) has made rapid progress on zero-shot indoor and outdoor scenes, powered by large-scale pre-training and vision transformers [8, 37, 74, 103, 113]. Even so, these models still struggle on weakly textured distant regions and on geometrically flat surfaces [28, 31, 80]. These are exactly the cases where defocus differences can supply an additional geometric signal that is independent of scene appearance [2, 7, 20, 95, 111]. These limitations call for a unified, physically grounded mechanism that exploits defocus as a reliable geometric cue without tying bokeh quality to a single depth estimator.

Our core insight is to *decouple bokeh synthesis from depth prediction and leverage defocus as a supervision-free geometric cue that enhances the accuracy and physical consistency of monocular depth estimation*. However, turning this idea into a practical system requires us to address several coupled challenges. We must enforce physically consistent and controllable depth-free bokeh [100], make defocus cues interpretable, calibratable and stable across domains [1, 88], integrate these signals safely with strong monocular depth foundations [74, 113], and prevent noisy or spurious blur from corrupting depth predictions [47]. We propose *BokehDepth*, a two stage framework shown in Figure 2 that first employs a physically grounded controllable depth-free bokeh generator to construct reliable bokeh stacks and then injects the resulting defocus cues into any monocular depth foundation model through a plug-and-play defocus-aware module inserted in the encoder.

In Stage-1, we build a physically guided yet depth-free

bokeh generator on top of a strong pretrained image-editing backbone [4]. We unify sparse real focus-defocus pairs, in-the-wild defocused photographs with lens metadata, and synthetic bokeh renderings by mapping their defocus level to a single thin-lens-derived control scalar that measures effective bokeh strength [25]. Conditioned on this scalar, Stage-1 produces from a single sharp input a compact bokeh stack with multiple calibrated defocus levels, without requiring any depth map. In Stage-2, we feed the Stage-1 bokeh stack and the original sharp frame into a discriminative monocular depth encoder. A lightweight defocus-aware aggregation module is inserted into the encoder to fuse features along the calibrated bokeh-strength axis, exposing depth-sensitive defocus variations while leaving the downstream decoder and metric head unchanged. This design lets us plug *BokehDepth* into strong monocular depth foundations and turn synthetic defocus cues into consistent gains in metric accuracy and physical consistency. We summarize our main contributions as follows:

- We design a bokeh renderer on top of powerful pretrained image editing backbone. Through a unified real and synthetic data pipeline and bokeh-conditioned adapters, Stage-1 generates reliable multi-strength bokeh stacks without using any depth map.
- We introduce a defocus-aware module that can be plugged into diverse monocular depth estimators. Given an input image and synthetic bokeh stack, it exposes stable defocus cues that enhance depth estimation.
- We show that combining Stage-1 and Stage-2 yields the *BokehDepth* framework, which improves visual fidelity over depth-map-based bokeh pipelines and consistently boosts the metric performance of strong monocular depth models across challenging indoor and outdoor scenes.

2. Related Works

2.1. Bokeh Synthesis

Defocus has been modeled with physically grounded camera and aperture formulations and with light field integration, which motivate filtering and layered reconstruction [45, 48, 49, 76, 98]. Depth map based image space rendering uses pyramidal filtering or per pixel layered splatting but struggles near discontinuities due to occlusion and color leakage [45, 48, 49]. Computational photography estimates

depth from stereo or dual pixel signals and then synthesizes shallow depth of field, yet remains sensitive to segmentation and disparity errors [3, 100]. Learning based pipelines train neural renderers for controllable bokeh, and physics guided hybrids reduce artifacts while retaining user control [38, 65, 77, 102, 108]. Differentiable and occlusion-aware renderers improve quality around edges, and layered scene representations such as multiplane images better handle partial occlusion, with extensions to video and mixed reality that enforce consistent lens characteristics [58, 66, 88, 89]. Generative diffusion methods inject strong image priors and explicit aperture conditioning to stabilize synthesis under imperfect depth and segmentation while enabling flexible refocusing and editing [25, 78, 104, 115, 124]. These advances indicate that diffusion models that embed camera physics offer an artifact resistant and scalable path to scene consistent bokeh across diverse imagery.

2.2. Monocular Depth Estimation

Recent advances in monocular depth estimation fall into two complementary streams, a discriminative feed forward family and a generative diffusion family. The discriminative stream begins with end to end models that adopt a scale invariant log loss [19] and then evolves to discretization and transformer based decoders such as DORN [26], AdaBins [5], NeW-CRFs [118], and iDisc [72]. Cross dataset transfer improves through large scale mixing in MegaDepth and MiDaS [50, 80], and ZoeDepth [6] connects relative training to metric prediction. Within this stream, camera aware modeling injects or normalizes intrinsics as in CAM-ConvS [22], canonicalization with geometry branches improves absolute scale in Metric3D [117] and Metric3Dv2 [35], and high resolution detail benefits from tile based inference in PatchFusion [51]. Data scaling and distillation further consolidate robustness, with Depth Anything [112] providing a broad foundation and Depth Anything V2 [113] advancing through synthetic replacement, stronger teachers, and large pseudo labeled real images. A current focus is universal monocular metric depth that targets absolute scale without test time camera metadata. UniDepth [73] and UniDepthV2 [74] adopt compact designs with learned camera representations, and Depth Pro [8] estimates field of view from image features to produce sharp metric maps at high resolution. The generative stream repurposes diffusion priors for depth, where Marigold adapts Stable Diffusion for affine invariant predictions with strong zero shot transfer [43], Diffusion-Depth [17] formulates depth as iterative denoising conditioned on the image, and Pixel Perfect Depth [109] performs diffusion in pixel space with semantics prompted transformers to strengthen edges and global consistency. Our approach follows the discriminative feed forward path for efficiency and reliability in universal metric depth while ac-

knowledging the strengths of diffusion models in fine structure and challenging appearance shifts.

3. Stage-1: Bokeh Generation

3.1. Background

We build Stage-1 on FLUX-Kontext [4], a rectified-flow transformer that unifies text-to-image generation and instruction-guided image editing in a single latent-space backbone [21, 54, 56]. Pretraining on large-scale editing tasks gives FLUX-Kontext strong priors for preserving structure, identity and photorealism under diverse manipulations [9, 60]. This property makes it an effective substrate for controllable, layout-aware bokeh editing without training a separate generator.

To connect FLUX-Kontext’s editing capacity to lens-like defocus, we ground our conditioning in the thin-lens circle-of-confusion model, inspired by the use of physical defocus parameters in Bokeh Diffusion [25] and related bokeh renderers [38, 58, 65, 66, 100, 114]. Under standard depth-of-field geometry, the CoC radius scales approximately linearly with the disparity offset from the focus plane [46], which motivates the pixel-space relation $r \approx K(f, N, S_1) \cdot \Delta\text{disp}$. We instantiate

$$K(f, N, S_1) = \frac{f^2 S_1}{2N(S_1 - f)} \cdot \text{pixel_ratio}, \quad (1)$$

where f and N are read from EXIF metadata, S_1 denotes the focus distance, Δdisp is the disparity offset from the focus plane, and pixel_ratio converts the CoC diameter into target pixel units [25]. In practice, this thin-lens relation is used only to derive a single calibrated scalar K that aligns real and synthetic defocus levels during training. At inference, Stage-1 is conditioned solely on this global K without access to any per-pixel depth or disparity map, so K functions as a unified and interpretable defocus-strength axis for depth-map-free and lens-consistent bokeh editing.

3.2. Unified Training with Real & Synthetic Bokeh

Stage-1 learns controllable, lens-consistent bokeh editing from a mixture of real photographs and synthetic renderings, all expressed through the physically grounded blur strength K defined in Equation (1). Our objective is to expose FLUX-Kontext to a wide variety of defocus patterns while preserving a single, interpretable control axis.

To exploit abundant in-the-wild images that lack dense all-in-focus pairs, we construct a text-to-image style corpus that follows the hybrid design of Bokeh Diffusion [25]. One subset contains natural photographs that exhibit authentic optical defocus. For these images we preserve EXIF metadata and compute a target K by combining thin-lens optics with off-the-shelf estimators [25]. The other subset contains sharp images that we augment with controllable

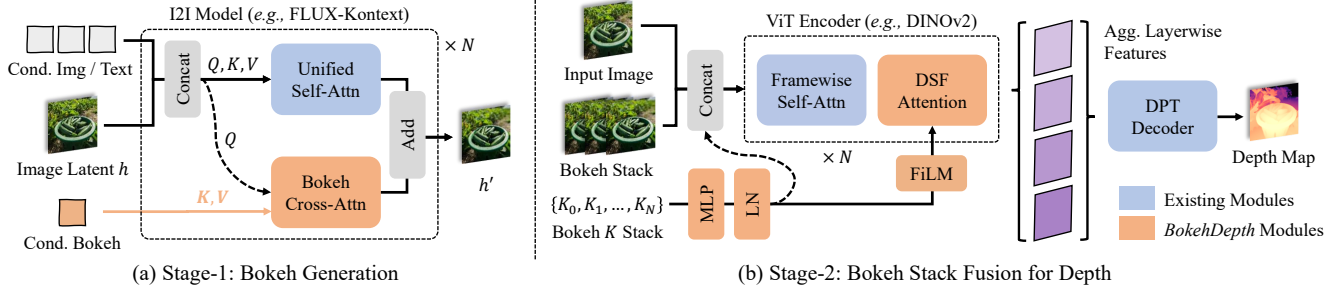


Figure 3. *BokehDepth* architecture. (a) Stage-1 bokeh generation augments a pretrained I2I model, such as FLUX-Kontext, with a bokeh cross-attention adapter that takes a scalar bokeh strength K and produces a calibrated multi-strength bokeh stack from a single sharp image. (b) Stage-2 bokeh stack fusion inserts Divided Space Focus (DSF) Attention into a ViT encoder and uses FiLM conditioning to inject the bokeh stack along the defocus axis, then feeds the aggregated layerwise features to an unchanged DPT decoder to predict metric depth.

shallow depth of field using physically motivated renderers BokehMe [65]. Each synthetic sample carries a known K . Representing both natural and rendered blur with the same scalar aligns their effective depth-of-field strength and encourages consistent bokeh behavior across domains.

For direct supervision we include limited paired datasets that record explicit focus or aperture changes, such as the BLB pairs from BokehMe [65], DPDD dual-pixel pairs [1], and the Aperture dataset [121]. Because the large-scale RealBokeh dataset [88] were released only recently, they were not available for the current experiments. We expect further gains once those pairs are incorporated in future training. All supervision sources are re-parameterized into the shared K domain using Equation (1), which aligns EXIF-derived optics, renderer settings, and estimated focus distance.

During training, Stage-1 alternates text-conditional and image-conditional objectives while conditioning exclusively on the unified blur scalar. At inference the model takes a single sharp image and a desired global K , and it produces a depth-map-free bokeh edit or a bokeh stack in a single batch. The resulting blur level is consistent across both real and synthetic regimes.

3.3. Bokeh Conditioning in MMDiT Attention

Our I2I pipeline is built on a Multimodal Diffusion Transformer (MMDiT) [21], in which both text tokens and latent image tokens are processed by a single unified self-attention block rather than separate self- and cross-attention modules as in the traditional U-Net architecture [36, 55, 83]. Concretely, let Q_T, K_T, V_T be the query, key, and value projections of the text tokens, and let Q_I, K_I, V_I be the projections of the current noisy latent image tokens after timestep dependent modulation. We first concatenate the text and image branches along the token dimension, apply rotary position embedding (RoPE) [94] to all queries and keys, and run one scaled dot-product attention over the joint sequence. We denote this unified attention mechanism as

$$h_{\text{MMDiT}} = \text{Attn}(\text{R}(Q_T \| Q_I), \text{R}(K_T \| K_I), V_T \| V_I), \quad (2)$$

where \parallel denotes concatenation along the token dimension, and $\text{R}(\cdot)$ denotes the application of RoPE. Inspired by Fortes et al. [25], we control defocus by introducing a dedicated bokeh branch. A single scalar bokeh strength K , which specifies the desired blur magnitude per unit-disparity, is passed through a small multilayer perceptron to produce a compact conditioning vector c_b . Two lightweight linear projections, implemented as LoRA adapters in practice, map c_b to a set of keys K_b and values V_b [25]. We reuse the same query that drives the unified attention in (2) and obtain a defocus-conditioned response

$$h_{\text{bokeh}} = \text{Attn}(\text{R}(Q_T \| Q_I), K_b, V_b). \quad (3)$$

The final hidden representation after each instrumented attention block is the sum of the original multimodal interaction and the bokeh response $h_{\text{final}} = h_{\text{MMDiT}} + \lambda h_{\text{bokeh}}$. This design enables the model to preserve the global scene layout and semantics from the image through h_{MMDiT} , while injecting a precise defocus control signal via h_{bokeh} . Remarkably, this elegant bokeh-attention mechanism works without any external depth map input, yet delivers effective bokeh rendering. The architecture follows the adapter-style conditioning paradigm introduced by IP-Adapter [116], but here it is integrated directly into the unified attention backbone of the MMDiT-based model in the I2I editing setting.

4. Stage-2: Bokeh Stack Fusion for Depth

4.1. Background

4.1.1. Depth from Defocus

Bokeh images intrinsically encode depth cues. Depth from defocus (DFD) is a long standing technique that recovers depth directly from defocus blur under a fixed viewpoint [27, 32, 59, 68, 90, 96, 97, 107, 110]. Stage-1 of our pipeline synthesizes a bokeh stack with different blur strengths K while keeping the scene, camera pose, and focus distance fixed. In theory, this stack alone is sufficient to reconstruct metric depth. We formalize this claim in the following proposition.

Proposition 1 (Depth-from-Bokeh Sweep under Calibrated Bokeh Control). *For a static scene observed by a thin-lens camera with fixed pose and focus distance, we record a bokeh stack by sweeping only the calibrated bokeh strength K . At every pixel, the measured bokeh radius is exactly proportional to that pixel’s inverse-depth offset from the focal plane. The slope of this proportionality, obtained by regressing radius on K across the stack, is an unbiased and consistent estimate of that offset and yields the pixel’s metric depth up to the usual front/behind-focus sign.*

A complete mathematical proof of Proposition 1 is given in supplementary material. The core advance over classical DfD is that Proposition 1 turns the defocus-to-depth relation into a per-pixel linear model and shows that the ordinary least squares slope of bokeh intensity K is an unbiased and statistically consistent estimator of the true inverse depth offset, which directly recovers metric depth at that pixel. In contrast, classical DfD typically takes two frames with different focus settings, estimates a blur radius, and then solves a fragile global optimization problem that needs strong priors and is sensitive to noise, weak texture, and calibration error [40, 70, 79, 86, 123, 125].

4.1.2. Discriminative Monocular Depth Estimation

Modern discriminative monocular depth estimation follows a feed-forward design in which a single transformer pass predicts dense metric depth from one RGB view, without multi-view optimization or iterative refinement [8, 74, 101, 113]. These systems use a large Vision Transformer encoder in the style of DINOv2 visual pretraining [15, 41, 63] together with a DPT-style decoder for dense prediction [81]. Let $I \in \mathbb{R}^{H \times W \times 3}$ be the input RGB image. The encoder E_θ produces a multi scale feature pyramid

$$\{F^{(s)}\}_{s=1}^S = E_\theta(I), \quad (4)$$

where each $F^{(s)}$ retains global semantic context and local detail through self-attention over the entire image. A DPT-style decoder D_ϕ then fuses and upsamples these features to recover a full resolution depth related field $\hat{z} = D_\phi(\{F^{(s)}\}_{s=1}^S)$, where $\hat{z}(p)$ denotes the predicted depth quantity at pixel p .

To express absolute metric scale, current feed-forward models attach a lightweight camera-aware head Γ_ψ that predicts viewing geometry from the same shared features. This head estimates camera parameters such as focal-length, per-ray direction, or full intrinsics and extrinsics. We write

$$\hat{D}_{\text{metric}}(p) = \text{Scale}\left(\hat{z}(p), \Gamma_\psi(\{F^{(s)}\}_{s=1}^S)(p)\right). \quad (5)$$

where $\hat{\kappa}$ is the inferred camera representation and $\text{Scale}(\cdot)$ converts \hat{z} into metric depth \hat{D}_{metric} in physical units. The key idea is that the network learns both scene and viewing geometry rather than applying scale afterward.

Training across this family of models emphasizes two goals. First, globally consistent metric scale across domains through camera-aware supervision and geometric consistency constraints; Second, sharp object boundaries and fine spatial detail through edge aware and multi-scale gradient losses, often distilled from high quality synthetic depth. As a result, these feed-forward estimators produce high resolution depth with crisp edges and reliable global scale from a single RGB frame in real time.

4.2. Divided Space Focus Attention in the Encoder

Our objective is to inject physically calibrated defocus cues into the discriminative monocular depth encoder while leaving the downstream decoder in Equation (5) unchanged. We assume a sharp reference RGB frame $I_0 \in \mathbb{R}^{H \times W \times 3}$ with bokeh strength $K_0 = 0$ and a synthetic bokeh stack $\{I_n\}_{n=1}^N$ produced by Stage-1 from the same viewpoint. Each I_n differs only in a controllable bokeh strength $K_n \in \mathbb{R}$. Following Equation (4), a shared vision transformer encoder E_θ processes every frame independently and returns per-frame patch tokens. We denote the tokens for frame n by $P_n \in \mathbb{R}^{K \times D}$ and collect them as $X = \{P_f\}_{f=0}^N \in \mathbb{R}^{(N+1) \times K \times D}$ together with the known strengths $\mathbf{K} = [K_0, \dots, K_N] \in \mathbb{R}^{(N+1) \times 1}$. Divided Space Focus Attention (DSFA) is inserted into encoder layers as an in-place feature rewriting block with **two steps**. **Step-1** performs spatial attention inside each frame. **Step-2** performs focus attention across frames at aligned spatial locations. After DSFA we retain only the refined tokens of the reference frame. The rest of the depth head can run exactly as in a standard single frame estimator.

Step-1: spatial attention within each frame. For each frame index $f \in \{0, \dots, N\}$ we embed the bokeh scalar K_f with a learnable multilayer perceptron (MLP) $g(\cdot)$:

$$t_f = g(K_f) \in \mathbb{R}^D. \quad (6)$$

We prepend t_f to that frame’s K patch tokens to obtain $S_f = [t_f; X_f] \in \mathbb{R}^{(1+K) \times D}$. We forward S_f through a transformer block and obtain

$$\tilde{S}_f = \text{FFN}(\text{MSA}(\text{LN}(S_f))) \in \mathbb{R}^{(1+K) \times D}. \quad (7)$$

Dropping the first token yields refined patch features $\tilde{X}_f = \tilde{S}_f[1:] \in \mathbb{R}^{K \times D}$ that encode how defocused the frame is.

Step-2: focus attention across frames. After spatial attention, we align patches across the stack. For each patch index j , we gather the same spatial location from all frames:

$$Y_j = [\tilde{X}_0[j], \tilde{X}_1[j], \dots, \tilde{X}_N[j]] \in \mathbb{R}^{(N+1) \times D}. \quad (8)$$

We modulate every element of Y_j with FiLM-style conditioning [18, 69, 93] from the same control tokens t_f . A

learned linear map $h(\cdot)$ predicts a per-frame scale and shift $[a_f, b_f] = h(t_f)$, $a_f, b_f \in \mathbb{R}^D$, and we apply channel wise affine modulation

$$\hat{Y}_{f,j} = (1 + \tanh(a_f)) \odot Y_{f,j} + b_f. \quad (9)$$

The modulated sequence $\hat{Y}_j \in \mathbb{R}^{(N+1) \times D}$ is then processed by multi-head self-attention along the frame axis. This lets each spatial location directly compare how blur changes as K varies, which is the physical depth-from-defocus cue. Accordingly, every frame receives refined tokens $\bar{X}_f \in \mathbb{R}^{K \times D}$. We keep the reference representation $Z = \bar{X}_0 \in \mathbb{R}^{K \times D}$. Finally, the dense prediction head from Equation (5) upsamples Z back to the pixel grid and outputs the metric depth map for the reference frame I_0 . In effect, DSFA injects the calibrated bokeh stack into the encoder while preserving the external interface of a standard monocular depth estimator. Together, Stages 1 and 2 constitute the overall *BokehDepth* pipeline, illustrated in Figure 3.

5. Experiments

5.1. Implementation Details

Stage-1. Following the unified training in Section 3.2, we train our FLUX-Kontext-based bokeh generator for 40 epochs at a fixed resolution of 512×512 , then run an additional 10 epochs using only I2I data at each dataset’s native resolution to adapt to heterogeneous image sizes. Training takes 7 days on $4 \times \text{A6000}$ GPUs. We compare against classical and neural baselines BokehMe [65], DrBokeh [89], BokehDiff [124], and the FLUX-Kontext editing backbone [4] on the exposure-aligned EBB! Val200 split [38, 67, 124]. To isolate the influence of depth prediction errors, we construct a synthetic SYNTHOBOKEH300 benchmark following prior protocols [65, 89, 124], where foreground and background layers from Lin et al. [53] are rendered with accurate depth maps. We report PSNR and SSIM for pixel-level and structural fidelity, and LPIPS [120] and DISTs [16] for perceptual similarity.

Stage-2. For metric depth estimation, we integrate the DSFA module into Depth Anything V2-L (DAv2) [113] and UniDepthV2-L (UDv2) [74]. We initialize from the official L-version checkpoints and fine-tune using each base model’s published training pipeline on bokeh stacks generated by our Stage-1. For cross-domain zero-shot MMDE, we fine-tune only on Hypersim [82], where each sharp frame is paired with its synthetic bokeh stack, and evaluate alongside strong baselines on diverse indoor and outdoor benchmarks following standard δ_1 and AbsRel protocols [8, 19, 35, 52, 62, 71, 74]. For in-domain evaluation, we use the NYUv2 [91] training split augmented with Stage-1 stacks and report results on the official test split.

5.2. Experimental Results

5.2.1. Stage-1: Bokeh Rendering

For real photographs, the quantitative results in Table 1 show that our method delivers the highest overall fidelity, with consistent gains in PSNR [30] and SSIM [105], and markedly lower LPIPS [120] and DISTs [16]. Notably, although some of our training examples were synthesized with BokehMe [65], the quality of our bokeh generation is not bounded by that renderer. We leverage FLUX-Kontext’s strong image-editing priors and the real bokeh datasets to produce synthesized defocus that faithfully matches lens-like optical behavior observed in real photography.

For synthetic scenes with reliable ground-truth depth, DrBokeh, which operates with direct access to depth and performs layered rendering, achieves the strongest PSNR. Our Stage-1 generator closely approaches these physically supervised baselines and attains the best perceptual quality across SSIM, LPIPS and DISTs. These results indicate that the unified, lens-derived control scalar K guides our model to reproduce the spatial structure and blur profiles prescribed by geometric optics, without requiring explicit depth maps at inference time.

Taken together, the real and synthetic evaluations in Table 1 and Figure 4 show that Stage-1 learns a robust and interpretable bokeh control space. The model retains the instruction-following flexibility of FLUX-Kontext while lifting it to a depth-map-free yet lens-consistent bokeh renderer that generalizes across diverse natural photographs and controlled layered scenes.

5.2.2. Stage-2: Monocular Metric Depth Estimation

We now examine how DSFA strengthens existing monocular metric depth models when they are guided by Stage-1 bokeh stacks. Each depth backbone receives the sharp input image together with a three-frame stack generated by Stage-1 at calibrated bokeh strengths $K \in \{10.0, 20.0, 30.0\}$, and DSFA aggregates these defocus cues without modifying the original decoder or loss design.

For cross-domain zero-shot MMDE in Table 2, the *BokehDepth* variants consistently achieve better or comparable AbsRel and δ_1 than strong baselines, while broadly improving each underlying model. These gains arise because DSFA operates along a physically normalised blur axis K rather than dataset-specific heuristics, which stabilises defocus cues across diverse scenes. On the in-domain NYUv2 benchmark, Table 3 shows that *BokehDepth* attains state-of-the-art error levels. The improvements are most pronounced on thin structures, reflective surfaces and cluttered indoor layouts where single-frame cues are ambiguous. DSFA leverages the structured variations in the bokeh stack to sharpen object boundaries and stabilise local metric scale, while preserving the favourable behaviour of the backbone models in well-conditioned regions.



Figure 4. Qualitative comparisons between our Stage-1 model, BokehMe [65], Dr. Bokeh [89], BokehDiff [124], FLUX-Kontext [4], and the ground truth. Our method more reliably preserves in-focus subjects while producing background blur that increases monotonically with depth. At depth discontinuities, it substantially reduces edge halos and color bleeding.

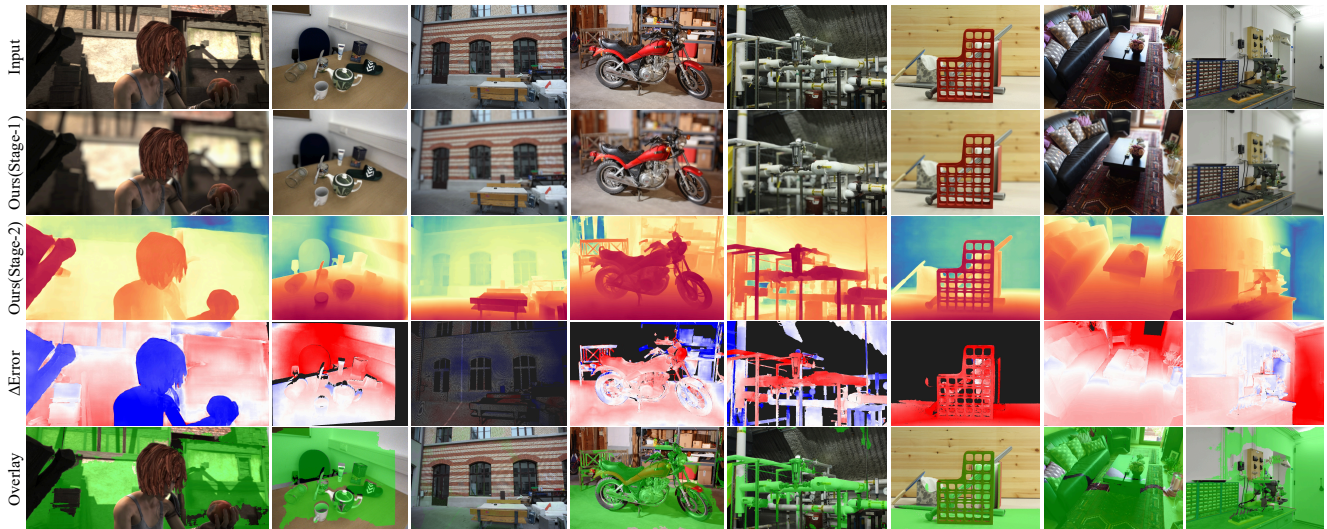


Figure 5. Qualitative results of *BokehDepth*. *Top to bottom*: input image, a frame from the Stage-1 bokeh stack, predicted depth by Stage-2, Δ Error maps showing per-pixel reduction in absolute depth error of *BokehDepth* relative to base model Depth Anything V2 [113], and RGB images overlaid with green highlights indicating improvement regions. *BokehDepth* lowers depth errors on fine structures, weakly-textured walls and distant background regions, offering more distinct layer separation and steadier metric depth across varied scenes.

Qualitative comparisons in Figure 5 further confirm that *BokehDepth* produces depth maps with clearer layer separation, cleaner occlusion boundaries and more reliable far-range estimates than single-frame counterparts, especially in cases where textures are weak but defocus changes remain informative. These results indicate that calibrated Stage-1 bokeh stacks together with the plug-and-play DSFA integration provide an effective bridge between learned defocus and universal MMDE.

5.3. Ablation Studies

Ablation on Stage-1 Bokeh Cross-Attention Design. By comparing FLUX-Kontext [4] and our *BokehDepth* re-

sults in Table 1, we conclude that the observed improvement in bokeh rendering originates from our Stage-1 Bokeh Cross-Attention design rather than from FLUX-Kontext’s text-driven image editing capabilities [25, 119]. The FLUX-Kontext base model performs poorly on physically consistent, lens-like defocus rendering. In contrast, our cross-attention design yields more accurate and visually coherent bokeh that better matches real optical defocus.

Ablation on Stage-2 Divided Space Focus Attention.

Table 4 ablates the main components of the Stage-2 DSFA module. *BokehDepth (w/o Focus)* keeps only the Space branch and removes the Focus branch. *BokehDepth (w/o*

Method	EBB! Val200 (real) [38, 67]				SystheBokeh300 (synthetic)			
	PSNR \uparrow	SSIM \uparrow	LPIPS \downarrow	DISTS \downarrow	PSNR \uparrow	SSIM \uparrow	LPIPS \downarrow	DISTS \downarrow
BokehMe [65]	24.1293	0.7511	0.3895	0.1431	22.8252	0.8085	0.2794	0.1884
DrBokeh [89]	22.6099	0.7353	0.4345	0.1782	29.7009	<u>0.8954</u>	<u>0.1494</u>	<u>0.0874</u>
BokehDiff [124]	<u>24.3466</u>	<u>0.8022</u>	0.2787	<u>0.1121</u>	26.2120	0.8065	0.2882	0.1417
FLUX-Kontext [4]	19.9225	0.6453	0.1654	0.4270	20.3375	0.6849	0.3514	0.1553
Ours	25.9084	0.8563	<u>0.1852</u>	0.0758	<u>29.1215</u>	0.9011	0.1385	0.0725

Table 1. Quantitative comparison on EBB! Val200 and SystheBokeh300. **Boldface** denotes the best and underline the second best.

Method	HAMMER [42]		IBims-1 [44]		Middlebury [85]		Make3D [84]		Sintel [10]		ETH3D [87]	
	$\delta_1 \uparrow$	Abs_rel \downarrow										
ZoeDepth [6]	0.009	0.943	0.672	0.174	0.538	<u>0.214</u>	0.649	0.221	0.078	0.946	0.338	0.500
Metric3Dv2 [34]	0.653	0.357	0.941	0.100	0.299	0.450	0.512	0.394	0.383	0.370	0.987	0.042
DepthPro [8]	0.630	0.391	0.823	0.159	0.605	0.251	0.728	0.254	0.400	0.508	0.415	0.327
DAv2 [113]	0.828	0.134	0.938	0.080	0.618	0.240	0.726	<u>0.217</u>	0.538	0.569	0.910	0.091
+ BokehDepth	<u>0.894</u>	<u>0.105</u>	<u>0.960</u>	<u>0.064</u>	<u>0.675</u>	0.215	<u>0.740</u>	0.206	<u>0.542</u>	0.413	0.954	0.077
UDv2 [74]	0.645	0.293	0.945	0.082	0.535	0.288	0.739	0.263	0.344	0.496	0.852	0.160
+ BokehDepth	0.895	0.094	0.978	0.039	0.716	0.205	0.786	0.228	0.671	<u>0.391</u>	<u>0.963</u>	<u>0.074</u>

Table 2. Zero-shot metric-depth comparison across diverse indoor and outdoor datasets. **Boldface** denotes the best result and underline denotes the second best. Our method consistently improves accuracy over each corresponding base model.

Method	Abs_Rel \downarrow	RMS \downarrow	Log ₁₀ \downarrow
ZoeDepth [6]	0.077	0.278	0.033
Metric3Dv2 [35]	<u>0.047</u>	0.183	<u>0.020</u>
DepthAnythingv2 [113]	0.056	0.206	0.024
UniDepthV2 [74]	<u>0.047</u>	<u>0.180</u>	<u>0.020</u>
BokehDepth (Ours)	0.039	0.043	0.016

Table 3. Metric depth comparison of *BokehDepth* (UniDepthV2 backbone) against other methods on the NYUv2 validation set [91]. All models were trained or fine-tuned on NYUv2.

Method	$\delta_1 \uparrow$	Abs_Rel \downarrow
Depth Anything v2 [113]	0.914	0.097
BokehDepth (w/o Focus)	0.620	0.215
BokehDepth (w/o Space)	0.567	0.236
BokehDepth (w/o FiLM)	0.602	0.223
BokehDepth (w/o Bokeh)	0.855	0.119
BokehDepth (w/ BokehMe)	0.914	0.094
BokehDepth (Ours)	0.943	0.084

Table 4. Ablation study of the Stage-2 Divided Space Focus Attention design. All methods are trained on VKITTI2 [11] and evaluated on the KITTI [29] Eigen split for metric depth. Each *BokehDepth* variant uses the same *Depth Anything v2* backbone and the same training protocol as the base model.

Space) drops the Space branch so the Focus branch alone performs cross-frame attention. *BokehDepth (w/o FiLM)*

keeps both branches but disables FiLM conditioning on the focus parameter k . *BokehDepth (w/o Bokeh)* repeats the all-in-focus image across the stack with $K = 0$, removing meaningful defocus variation. *BokehDepth (w/ BokehMe)* feeds DSFA with bokeh stacks rendered by BokehMe [65] from ground-truth depth instead of Stage-1 outputs. Taken together, these controlled variants show that the gains in metric depth depend on both branches of DSFA and on accurate, calibrated bokeh stacks from Stage-1.

6. Conclusion

BokehDepth asks whether lens-aware defocus, grounded in thin-lens physics and powered by a pretrained image-editing prior, can act as a depth-map-free geometric cue for monocular metric depth. We propose a two-stage framework that first learns a controllable bokeh generator on FLUX-Kontext to synthesize calibrated bokeh stacks without depth maps, and then feeds these stacks into existing depth encoders through a plug-and-play Divided Space Focus Attention module. Across real and synthetic bokeh benchmarks and diverse indoor and outdoor depth datasets, this design improves visual fidelity over depth-based bokeh pipelines and consistently boosts strong monocular depth foundations in both in-domain and zero-shot settings. These results suggest that physically guided defocus can serve as a scalable and supervision-free signal that complements large image backbones and moves toward unified models that jointly learn image formation, defocus and depth.

References

- [1] Abdullah Abuolaim and Michael S Brown. Defocus deblurring using dual-pixel data. In *European conference on computer vision*, pages 111–126. Springer, 2020. 2, 4
- [2] Edward H Adelson and John YA Wang. Single lens stereo with a plenoptic camera. *IEEE transactions on pattern analysis and machine intelligence*, 14(2):99–106, 1992. 2
- [3] Jonathan T Barron, Andrew Adams, YiChang Shih, and Carlos Hernández. Fast bilateral-space stereo for synthetic defocus. In *Proceedings of the IEEE conference on computer vision and pattern recognition*, pages 4466–4474, 2015. 3
- [4] Stephen Batifol, Andreas Blattmann, Frederic Boesel, Saksham Consul, Cyril Diagne, Tim Dockhorn, Jack English, Zion English, Patrick Esser, Sumith Kulal, et al. Flux. 1 kontext: Flow matching for in-context image generation and editing in latent space. *arXiv e-prints*, pages arXiv:2506.2025. 2, 3, 6, 7, 8, 1, 4, 5
- [5] Shariq Farooq Bhat, Ibraheem Alhashim, and Peter Wonka. Adabins: Depth estimation using adaptive bins. In *Proceedings of the IEEE/CVF conference on computer vision and pattern recognition*, pages 4009–4018, 2021. 3
- [6] Shariq Farooq Bhat, Reiner Birkel, Diana Wofk, Peter Wonka, and Matthias Müller. Zoedepth: Zero-shot transfer by combining relative and metric depth. *arXiv preprint arXiv:2302.12288*, 2023. 3, 8
- [7] Ilya Blayvas, Ron Kimmel, and Ehud Rivlin. Role of optics in the accuracy of depth-from-defocus systems. *Journal of the Optical Society of America A*, 24(4):967–972, 2007. 2
- [8] Aleksei Bochkovskii, Amaël Delaunoy, Hugo Germain, Marcel Santos, Yichao Zhou, Stephan R Richter, and Vladlen Koltun. Depth pro: Sharp monocular metric depth in less than a second. *arXiv preprint arXiv:2410.02073*, 2024. 2, 3, 5, 6, 8
- [9] Tim Brooks, Aleksander Holynski, and Alexei A Efros. Instructpix2pix: Learning to follow image editing instructions. In *Proceedings of the IEEE/CVF conference on computer vision and pattern recognition*, pages 18392–18402, 2023. 3
- [10] Daniel J Butler, Jonas Wulff, Garrett B Stanley, and Michael J Black. A naturalistic open source movie for optical flow evaluation. In *European conference on computer vision*, pages 611–625. Springer, 2012. 8
- [11] Johann Cabon, Naila Murray, and Martin Humenberger. Virtual kitti 2. *arXiv preprint arXiv:2001.10773*, 2020. 8
- [12] Subhasis Chaudhuri and Ambajagan N Rajagopalan. *Depth from defocus: a real aperture imaging approach*. Springer Science & Business Media, 1999. 2
- [13] Junsong Chen, Jincheng Yu, Chongjian Ge, Lewei Yao, Enze Xie, Yue Wu, Zhongdao Wang, James Kwok, Ping Luo, Huchuan Lu, et al. Pixart- α : Fast training of diffusion transformer for photorealistic text-to-image synthesis. *arXiv preprint arXiv:2310.00426*, 2023. 1
- [14] Junsong Chen, Chongjian Ge, Enze Xie, Yue Wu, Lewei Yao, Xiaoze Ren, Zhongdao Wang, Ping Luo, Huchuan Lu, and Zhenguo Li. Pixart- σ : Weak-to-strong training of diffusion transformer for 4k text-to-image generation. In *European Conference on Computer Vision*, pages 74–91. Springer, 2024. 1
- [15] Timothée Darcet, Maxime Oquab, Julien Mairal, and Piotr Bojanowski. Vision transformers need registers, 2023. 5
- [16] Keyan Ding, Kede Ma, Shiqi Wang, and Eero P Simoncelli. Image quality assessment: Unifying structure and texture similarity. *IEEE transactions on pattern analysis and machine intelligence*, 44(5):2567–2581, 2020. 6, 7
- [17] Yiquan Duan, Xianda Guo, and Zheng Zhu. Diffusion-depth: Diffusion denoising approach for monocular depth estimation. In *European Conference on Computer Vision*, pages 432–449. Springer, 2024. 3
- [18] Vincent Dumoulin, Ethan Perez, Nathan Schucher, Florian Strub, Harm de Vries, Aaron Courville, and Yoshua Bengio. Feature-wise transformations. *Distill*, 3(7):e11, 2018. 5
- [19] David Eigen, Christian Puhrsch, and Rob Fergus. Depth map prediction from a single image using a multi-scale deep network. *Advances in neural information processing systems*, 27, 2014. 1, 3, 6
- [20] John Ens and Peter Lawrence. An investigation of methods for determining depth from focus. *IEEE Transactions on pattern analysis and machine intelligence*, 15(2):97–108, 2002. 2
- [21] Patrick Esser, Sumith Kulal, Andreas Blattmann, Rahim Entezari, Jonas Müller, Harry Saini, Yam Levi, Dominik Lorenz, Axel Sauer, Frederic Boesel, et al. Scaling rectified flow transformers for high-resolution image synthesis. In *Forty-first international conference on machine learning*, 2024. 3, 4, 1
- [22] Jose M Facil, Benjamin Ummenhofer, Huizhong Zhou, Luis Montesano, Thomas Brox, and Javier Civera. Camconvs: Camera-aware multi-scale convolutions for single-view depth. In *Proceedings of the IEEE/CVF conference on computer vision and pattern recognition*, pages 11826–11835, 2019. 3
- [23] Paolo Favaro and Stefano Soatto. A geometric approach to shape from defocus. *IEEE Transactions on Pattern Analysis and Machine Intelligence*, 27(3):406–417, 2005. 2
- [24] Paolo Favaro, Stefano Soatto, Martin Burger, and Stanley J Osher. Shape from defocus via diffusion. *IEEE transactions on pattern analysis and machine intelligence*, 30(3): 518–531, 2008. 2
- [25] Armando Fortes, Tianyi Wei, Shangchen Zhou, and Xingang Pan. Bokeh diffusion: Defocus blur control in text-to-image diffusion models. *arXiv preprint arXiv:2503.08434*, 2025. 1, 2, 3, 4, 7
- [26] Huan Fu, Mingming Gong, Chaohui Wang, Kayhan Batmanghelich, and Dacheng Tao. Deep ordinal regression network for monocular depth estimation. In *Proceedings of the IEEE conference on computer vision and pattern recognition*, pages 2002–2011, 2018. 3
- [27] Yuki Fujimura, Masaaki Iiyama, Takuya Funatomi, and Yasuhiro Mukaigawa. Deep depth from focal stack with defocus model for camera-setting invariance. *International Journal of Computer Vision*, 132(6):1970–1985, 2024. 4
- [28] Stefano Gasperini, Nils Morbitzer, HyunJun Jung, Nassir Navab, and Federico Tombari. Robust monocular depth

- estimation under challenging conditions. In *Proceedings of the IEEE/CVF international conference on computer vision*, pages 8177–8186, 2023. 2
- [29] Andreas Geiger, Philip Lenz, and Raquel Urtasun. Are we ready for autonomous driving? the kitti vision benchmark suite. In *2012 IEEE conference on computer vision and pattern recognition*, pages 3354–3361. IEEE, 2012. 8
- [30] Rafael C Gonzalez. *Digital image processing*. Pearson education india, 2009. 6
- [31] Yuliang Guo, Sparsh Garg, S Mahdi H Miangoleh, Xinyu Huang, and Liu Ren. Depth any camera: Zero-shot metric depth estimation from any camera. In *Proceedings of the Computer Vision and Pattern Recognition Conference*, pages 26996–27006, 2025. 2
- [32] Caner Hazirbas, Sebastian Georg Soyer, Maximilian Christian Staab, Laura Leal-Taixé, and Daniel Cremers. Deep depth from focus. In *Asian conference on computer vision*, pages 525–541. Springer, 2018. 4
- [33] Jonathan Ho, Ajay Jain, and Pieter Abbeel. Denoising diffusion probabilistic models. *Advances in neural information processing systems*, 33:6840–6851, 2020. 1
- [34] Mu Hu, Wei Yin, Chi Zhang, Zhipeng Cai, Xiaoxiao Long, Hao Chen, Kaixuan Wang, Gang Yu, Chunhua Shen, and Shaojie Shen. Metric3d v2: A versatile monocular geometric foundation model for zero-shot metric depth and surface normal estimation. *IEEE Transactions on Pattern Analysis and Machine Intelligence*, 2024. 8
- [35] Mu Hu, Wei Yin, Chi Zhang, Zhipeng Cai, Xiaoxiao Long, Hao Chen, Kaixuan Wang, Gang Yu, Chunhua Shen, and Shaojie Shen. Metric3d v2: A versatile monocular geometric foundation model for zero-shot metric depth and surface normal estimation. *IEEE Transactions on Pattern Analysis and Machine Intelligence*, 2024. 3, 6, 8
- [36] Litao Hua, Fan Liu, Jie Su, Xingyu Miao, Zizhou Ouyang, Zeyu Wang, Runze Hu, Zhenyu Wen, Bing Zhai, Yang Long, et al. Attention in diffusion model: A survey. *arXiv preprint arXiv:2504.03738*, 2025. 4
- [37] Zhiwei Huang, Mohammed AH Ali, Yusoff Nukman, Hai Lu Xu, Shikai Zhang, Hui Chen, and Mohammad Alkhedher. A systematic review of monocular depth estimation for autonomous driving: Methods and dataset benchmarking. *Results in Engineering*, page 105359, 2025. 2
- [38] Andrey Ignatov, Jagruti Patel, and Radu Timofte. Rendering natural camera bokeh effect with deep learning. In *Proceedings of the IEEE/CVF Conference on Computer Vision and Pattern Recognition Workshops*, pages 418–419, 2020. 3, 6, 8, 5
- [39] Hayato Ikoma, Cindy M Nguyen, Christopher A Metzler, Yifan Peng, and Gordon Wetzstein. Depth from defocus with learned optics for imaging and occlusion-aware depth estimation. In *2021 IEEE International Conference on Computational Photography (ICCP)*, pages 1–12. IEEE, 2021. 2
- [40] Hailin Jin and Paolo Favaro. A variational approach to shape from defocus. In *European Conference on Computer Vision*, pages 18–30. Springer, 2002. 5
- [41] Cijo Jose, Théo Moutakanni, Dahyun Kang, Federico Baldassarre, Timothée Darcet, Hu Xu, Daniel Li, Marc Szafranec, Michaël Ramamonjisoa, Maxime Oquab, Oriane Siméoni, Huy V. Vo, Patrick Labatut, and Piotr Bojanowski. Dinov2 meets text: A unified framework for image- and pixel-level vision-language alignment, 2024. 5
- [42] HyunJun Jung, Patrick Ruhkamp, Guangyao Zhai, Nikolas Brasch, Yitong Li, Yannick Verdie, Jifei Song, Yiren Zhou, Anil Armagan, Slobodan Ilic, et al. Is my depth ground-truth good enough? hammer—highly accurate multi-modal dataset for dense 3d scene regression. *arXiv preprint arXiv:2205.04565*, 2022. 8
- [43] Bingxin Ke, Anton Obukhov, Shengyu Huang, Nando Metzger, Rodrigo Caye Daudt, and Konrad Schindler. Repurposing diffusion-based image generators for monocular depth estimation. In *Proceedings of the IEEE/CVF conference on computer vision and pattern recognition*, pages 9492–9502, 2024. 3
- [44] Tobias Koch, Lukas Liebel, Friedrich Fraundorfer, and Marco Korner. Evaluation of cnn-based single-image depth estimation methods. In *Proceedings of the European Conference on Computer Vision (ECCV) Workshops*, pages 0–0, 2018. 8
- [45] Martin Kraus and Magnus Strengert. Depth-of-field rendering by pyramidal image processing. In *Computer graphics forum*, pages 645–654. Wiley Online Library, 2007. 2
- [46] Reginald L Lagendijk and Jan Biemond. Basic methods for image restoration and identification. In *The essential guide to image processing*, pages 323–348. Elsevier, 2009. 3, 1, 2
- [47] Junyong Lee, Hyeongseok Son, Jaesung Rim, Sunghyun Cho, and Seungyong Lee. Iterative filter adaptive network for single image defocus deblurring. In *Proceedings of the IEEE/CVF conference on computer vision and pattern recognition*, pages 2034–2042, 2021. 2
- [48] Sungkil Lee, Gerard Jounghyun Kim, and Seungmoon Choi. Real-time depth-of-field rendering using point splatting on per-pixel layers. In *Computer Graphics Forum*, pages 1955–1962. Wiley Online Library, 2008. 2
- [49] Sungkil Lee, Elmar Eisemann, and Hans-Peter Seidel. Real-time lens blur effects and focus control. *ACM Transactions on Graphics (TOG)*, 29(4):1–7, 2010. 2
- [50] Zhengqi Li and Noah Snavely. Megadepth: Learning single-view depth prediction from internet photos. In *Proceedings of the IEEE conference on computer vision and pattern recognition*, pages 2041–2050, 2018. 3
- [51] Zhenyu Li, Shariq Farooq Bhat, and Peter Wonka. Patchfusion: An end-to-end tile-based framework for high-resolution monocular metric depth estimation. In *Proceedings of the IEEE/CVF Conference on Computer Vision and Pattern Recognition*, pages 10016–10025, 2024. 3
- [52] Zhenyu Li, Haotong Lin, Jiashi Feng, Peter Wonka, and Bingyi Kang. Benchdepth: Are we on the right way to evaluate depth foundation models? *arXiv preprint arXiv:2507.15321*, 2025. 6
- [53] Shanchuan Lin, Andrey Ryabtsev, Soumyadip Sengupta, Brian L Curless, Steven M Seitz, and Ira Kemelmacher-Shlizerman. Real-time high-resolution background mat-

- ting. In *Proceedings of the IEEE/CVF Conference on Computer Vision and Pattern Recognition*, pages 8762–8771, 2021. 6
- [54] Yaron Lipman, Ricky TQ Chen, Heli Ben-Hamu, Maximilian Nickel, and Matt Le. Flow matching for generative modeling. *arXiv preprint arXiv:2210.02747*, 2022. 3
- [55] Bingyan Liu, Chengyu Wang, Tingfeng Cao, Kui Jia, and Jun Huang. Towards understanding cross and self-attention in stable diffusion for text-guided image editing. In *Proceedings of the IEEE/CVF conference on computer vision and pattern recognition*, pages 7817–7826, 2024. 4
- [56] Xingchao Liu, Chengyue Gong, and Qiang Liu. Flow straight and fast: Learning to generate and transfer data with rectified flow. *arXiv preprint arXiv:2209.03003*, 2022. 3, 1
- [57] Xianrui Luo, Juewen Peng, Ke Xian, Zijin Wu, and Zhiguo Cao. Defocus to focus: Photo-realistic bokeh rendering by fusing defocus and radiance priors. *Information Fusion*, 89: 320–335, 2023. 2
- [58] David Mandl, Shohei Mori, Peter Mohr, Yifan Peng, Tobias Langlotz, Dieter Schmalstieg, and Denis Kalkofen. Neural bokeh: Learning lens blur for computational videography and out-of-focus mixed reality. In *2024 IEEE Conference Virtual Reality and 3D User Interfaces (VR)*, pages 870–880. IEEE, 2024. 1, 2, 3
- [59] Maxim Maximov, Kevin Galim, and Laura Leal-Taixé. Focus on defocus: bridging the synthetic to real domain gap for depth estimation. In *Proceedings of the IEEE/CVF conference on computer vision and pattern recognition*, pages 1071–1080, 2020. 4
- [60] Chenlin Meng, Yutong He, Yang Song, Jiaming Song, Jiajun Wu, Jun-Yan Zhu, and Stefano Ermon. Sdedit: Guided image synthesis and editing with stochastic differential equations. *arXiv preprint arXiv:2108.01073*, 2021. 3
- [61] Shree K Nayar, Masahiro Watanabe, and Minoru Noguchi. Real-time focus range sensor. *IEEE Transactions on Pattern Analysis and Machine Intelligence*, 18(12):1186–1198, 2002. 2
- [62] Anton Obukhov, Matteo Poggi, Fabio Tosi, Ripudaman Singh Arora, Jaime Spencer, Chris Russel, Simon Hadfield, Richard Bowden, Shuaihang Wang, Zhenxin Ma, et al. The fourth monocular depth estimation challenge. In *Proceedings of the Computer Vision and Pattern Recognition Conference*, pages 6182–6195, 2025. 6
- [63] Maxime Oquab, Timothée Darcet, Theo Moutakanni, Huy V. Vo, Marc Szafraniec, Vasil Khalidov, Pierre Fernandez, Daniel Haziza, Francisco Massa, Alaaeldin El-Nouby, Russell Howes, Po-Yao Huang, Hu Xu, Vasu Sharma, Shang-Wen Li, Wojciech Galuba, Mike Rabbat, Mido Assran, Nicolas Ballas, Gabriel Synnaeve, Ishan Misra, Herve Jegou, Julien Mairal, Patrick Labatut, Armand Joulin, and Piotr Bojanowski. DINOv2: Learning robust visual features without supervision, 2023. 5
- [64] Juewen Peng, Xianrui Luo, Ke Xian, and Zhiguo Cao. Interactive portrait bokeh rendering system. In *2021 IEEE International Conference on Image Processing (ICIP)*, pages 2923–2927. IEEE, 2021. 2
- [65] Juewen Peng, Zhiguo Cao, Xianrui Luo, Hao Lu, Ke Xian, and Jianming Zhang. Bokehme: When neural rendering meets classical rendering. In *Proceedings of the IEEE/CVF conference on computer vision and pattern recognition*, pages 16283–16292, 2022. 2, 3, 4, 6, 7, 8, 1, 5
- [66] Juewen Peng, Jianming Zhang, Xianrui Luo, Hao Lu, Ke Xian, and Zhiguo Cao. Mpib: An mpi-based bokeh rendering framework for realistic partial occlusion effects. In *Computer Vision – ECCV 2022*. Springer, 2022. 2, 3
- [67] Juewen Peng, Zhiyu Pan, Chengxin Liu, Xianrui Luo, Huiqiang Sun, Liao Shen, Ke Xian, and Zhiguo Cao. Selective bokeh effect transformation. In *Proceedings of the IEEE/CVF conference on computer vision and pattern recognition*, pages 1456–1464, 2023. 6, 8, 5
- [68] Alex Paul Pentland. A new sense for depth of field. *IEEE transactions on pattern analysis and machine intelligence*, 11(4):523–531, 1987. 2, 4
- [69] Ethan Perez, Florian Strub, Harm De Vries, Vincent Dumoulin, and Aaron Courville. Film: Visual reasoning with a general conditioning layer. In *Proceedings of the AAAI conference on artificial intelligence*, 2018. 5
- [70] Nico Persch, Christopher Schroers, Simon Setzer, and Joachim Weickert. Introducing more physics into variational depth-from-defocus. In *German Conference on Pattern Recognition*, pages 15–27. Springer, 2014. 5
- [71] Duc-Hai Pham, Tung Do, Phong Nguyen, Binh-Son Hua, Khoi Nguyen, and Rang Nguyen. Sharpdepth: Sharpening metric depth predictions using diffusion distillation. In *Proceedings of the Computer Vision and Pattern Recognition Conference*, pages 17060–17069, 2025. 6
- [72] Luigi Piccinelli, Christos Sakaridis, and Fisher Yu. idisc: Internal discretization for monocular depth estimation. In *Proceedings of the IEEE/CVF Conference on Computer Vision and Pattern Recognition*, pages 21477–21487, 2023. 3
- [73] Luigi Piccinelli, Yung-Hsu Yang, Christos Sakaridis, Mattia Segu, Siyuan Li, Luc Van Gool, and Fisher Yu. Unidepth: Universal monocular metric depth estimation. In *Proceedings of the IEEE/CVF Conference on Computer Vision and Pattern Recognition*, pages 10106–10116, 2024. 3
- [74] Luigi Piccinelli, Christos Sakaridis, Yung-Hsu Yang, Mattia Segu, Siyuan Li, Wim Abbeloos, and Luc Van Gool. Unidepthv2: Universal monocular metric depth estimation made simpler. *arXiv preprint arXiv:2502.20110*, 2025. 1, 2, 3, 5, 6, 8
- [75] Dustin Podell, Zion English, Kyle Lacey, Andreas Blattmann, Tim Dockhorn, Jonas Müller, Joe Penna, and Robin Rombach. Sdxl: Improving latent diffusion models for high-resolution image synthesis. *arXiv preprint arXiv:2307.01952*, 2023. 1
- [76] Michael Potmesil and Indranil Chakravarty. A lens and aperture camera model for synthetic image generation. *ACM SIGGRAPH Computer Graphics*, 15(3):297–305, 1981. 2
- [77] Ming Qian, Congyu Qiao, Jiamin Lin, Zhenyu Guo, Chenghua Li, Cong Leng, and Jian Cheng. Bggan: Bokeh-glass generative adversarial network for rendering realistic

- bokeh. In *European Conference on Computer Vision*, pages 229–244. Springer, 2020. 3
- [78] Xinran Qin, Zhixin Wang, Fan Li, Haoyu Chen, Renjing Pei, Wenbo Li, and Xiaochun Cao. Camedit: Continuous camera parameter control for photorealistic image editing. In *The Thirty-ninth Annual Conference on Neural Information Processing Systems*, 2025. 3
- [79] AN Rajagopalan and Subhasis Chaudhuri. A variational approach to recovering depth from defocused images. *IEEE transactions on pattern analysis and machine intelligence*, 19(10):1158–1164, 2002. 5
- [80] René Ranftl, Katrin Lasinger, David Hafner, Konrad Schindler, and Vladlen Koltun. Towards robust monocular depth estimation: Mixing datasets for zero-shot cross-dataset transfer. *IEEE transactions on pattern analysis and machine intelligence*, 44(3):1623–1637, 2020. 1, 2, 3
- [81] René Ranftl, Alexey Bochkovskiy, and Vladlen Koltun. Vision transformers for dense prediction. In *Proceedings of the IEEE/CVF international conference on computer vision*, pages 12179–12188, 2021. 5
- [82] Mike Roberts, Jason Ramapuram, Anurag Ranjan, Atulit Kumar, Miguel Angel Bautista, Nathan Paczan, Russ Webb, and Joshua M Susskind. Hypersim: A photorealistic synthetic dataset for holistic indoor scene understanding. In *Proceedings of the IEEE/CVF international conference on computer vision*, pages 10912–10922, 2021. 6
- [83] Robin Rombach, Andreas Blattmann, Dominik Lorenz, Patrick Esser, and Björn Ommer. High-resolution image synthesis with latent diffusion models. In *Proceedings of the IEEE/CVF conference on computer vision and pattern recognition*, pages 10684–10695, 2022. 4, 1
- [84] Ashutosh Saxena, Min Sun, and Andrew Y Ng. Make3d: Learning 3d scene structure from a single still image. *IEEE transactions on pattern analysis and machine intelligence*, 31(5):824–840, 2008. 1, 8
- [85] Daniel Scharstein, Heiko Hirschmüller, York Kitajima, Greg Krathwohl, Nera Nešić, Xi Wang, and Porter Westling. High-resolution stereo datasets with subpixel-accurate ground truth. In *German conference on pattern recognition*, pages 31–42. Springer, 2014. 8
- [86] Yoav Y Schechner and Nahum Kiryati. Depth from defocus vs. stereo: How different really are they? *International Journal of Computer Vision*, 39(2):141–162, 2000. 5
- [87] Thomas Schops, Johannes L Schonberger, Silvano Galliani, Torsten Sattler, Konrad Schindler, Marc Pollefeys, and Andreas Geiger. A multi-view stereo benchmark with high-resolution images and multi-camera videos. In *Proceedings of the IEEE conference on computer vision and pattern recognition*, pages 3260–3269, 2017. 8
- [88] Tim Seizinger, Florin-Alexandru Vasluianu, Marcos V Conde, Zongwei Wu, and Radu Timofte. Bokehlicious: Photorealistic bokeh rendering with controllable apertures. *arXiv preprint arXiv:2503.16067*, 2025. 1, 2, 3, 4
- [89] Yichen Sheng, Zixun Yu, Lu Ling, Zhiwen Cao, Xuaner Zhang, Xin Lu, Ke Xian, Haiting Lin, and Bedrich Benes. Dr. bokeh: Differentiable occlusion-aware bokeh rendering. In *Proceedings of the IEEE/CVF Conference on Computer Vision and Pattern Recognition*, pages 4515–4525, 2024. 2, 3, 6, 7, 8, 1, 4, 5
- [90] Haozhe Si, Bin Zhao, Dong Wang, Yunpeng Gao, Mulin Chen, Zhigang Wang, and Xuelong Li. Fully self-supervised depth estimation from defocus clue. In *Proceedings of the IEEE/CVF Conference on Computer Vision and Pattern Recognition*, pages 9140–9149, 2023. 4
- [91] Nathan Silberman, Derek Hoiem, Pushmeet Kohli, and Rob Fergus. Indoor segmentation and support inference from rgbd images. In *European conference on computer vision*, pages 746–760. Springer, 2012. 6, 8
- [92] Jascha Sohl-Dickstein, Eric Weiss, Niru Maheswaranathan, and Surya Ganguli. Deep unsupervised learning using nonequilibrium thermodynamics. In *International conference on machine learning*, pages 2256–2265. pmlr, 2015. 1
- [93] Florian Strub, Mathieu Seurin, Ethan Perez, Harm De Vries, Jérémie Mary, Philippe Preux, and Aaron CourvilleOlivier Pietquin. Visual reasoning with multi-hop feature modulation. In *Proceedings of the European Conference on Computer Vision (ECCV)*, pages 784–800, 2018. 5
- [94] Jianlin Su, Murtadha Ahmed, Yu Lu, Shengfeng Pan, Wen Bo, and Yunfeng Liu. Roformer: Enhanced transformer with rotary position embedding. *Neurocomputing*, 568: 127063, 2024. 4, 1
- [95] Murali Subbarao and Gopal Surya. Depth from defocus: A spatial domain approach. *International Journal of computer vision*, 13(3):271–294, 1994. 2
- [96] Supasorn Suwajanakorn, Carlos Hernandez, and Steven M Seitz. Depth from focus with your mobile phone. In *Proceedings of the IEEE conference on computer vision and pattern recognition*, pages 3497–3506, 2015. 4
- [97] Huixuan Tang, Scott Cohen, Brian Price, Stephen Schiller, and Kiriakos N Kutulakos. Depth from defocus in the wild. In *Proceedings of the IEEE conference on computer vision and pattern recognition*, pages 2740–2748, 2017. 2, 4
- [98] Karthik Vaidyanathan, Jacob Munkberg, Petrik Clarberg, and Marco Salvi. Layered light field reconstruction for defocus blur. *ACM Transactions on Graphics (TOG)*, 34(2): 1–12, 2015. 2
- [99] Ashish Vaswani, Noam Shazeer, Niki Parmar, Jakob Uszkoreit, Llion Jones, Aidan N Gomez, Łukasz Kaiser, and Illia Polosukhin. Attention is all you need. *Advances in neural information processing systems*, 30, 2017. 1
- [100] Neal Wadhwa, Rahul Garg, David E Jacobs, Bryan E Feldman, Nori Kanazawa, Robert Carroll, Yair Movshovitz-Attias, Jonathan T Barron, Yael Pritch, and Marc Levoy. Synthetic depth-of-field with a single-camera mobile phone. *ACM Transactions on Graphics (ToG)*, 37(4):1–13, 2018. 2, 3, 1
- [101] Jianyuan Wang, Minghao Chen, Nikita Karaev, Andrea Vedaldi, Christian Rupprecht, and David Novotny. Vggt: Visual geometry grounded transformer. In *Proceedings of the Computer Vision and Pattern Recognition Conference*, pages 5294–5306, 2025. 5
- [102] Lijun Wang, Xiaohui Shen, Jianming Zhang, Oliver Wang, Zhe Lin, Chih-Yao Hsieh, Sarah Kong, and Huchuan Lu.

- Deeplens: Shallow depth of field from a single image. *arXiv preprint arXiv:1810.08100*, 2018. 3
- [103] Ruicheng Wang, Sicheng Xu, Yue Dong, Yu Deng, Jianfeng Xiang, Zelong Lv, Guangzhong Sun, Xin Tong, and Jiaolong Yang. Moge-2: Accurate monocular geometry with metric scale and sharp details. *arXiv preprint arXiv:2507.02546*, 2025. 2
- [104] Yiyang Wang, Xi Chen, Xiaogang Xu, Yu Liu, and Hengshuang Zhao. Diffcamera: Arbitrary refocusing on images. *arXiv preprint arXiv:2509.26599*, 2025. 3
- [105] Zhou Wang, Alan C Bovik, Hamid R Sheikh, and Eero P Simoncelli. Image quality assessment: from error visibility to structural similarity. *IEEE transactions on image processing*, 13(4):600–612, 2004. 6, 7
- [106] Masahiro Watanabe and Shree K Nayar. Telecentric optics for constant magnification imaging. *IEEE Trans. Pattern Anal. Mach. Intell.*, 19:1360–1365, 1995. 2
- [107] Lahiru Wijayasingha, Homa Alemzadeh, and John A Stankovic. Camera-independent single image depth estimation from defocus blur. In *Proceedings of the IEEE/CVF Winter Conference on Applications of Computer Vision*, pages 3749–3758, 2024. 2, 4
- [108] Lei Xiao, Anton Kaplanyan, Alexander Fix, Matt Chapman, and Douglas Lanman. Deepfocus: Learned image synthesis for computational display. In *ACM SIGGRAPH 2018 Talks*, pages 1–2. ACM SIGGRAPH, 2018. 3
- [109] Gangwei Xu, Haotong Lin, Hongcheng Luo, Xianqi Wang, Jingfeng Yao, Lianghui Zhu, Yuechuan Pu, Cheng Chi, Haiyang Sun, Bing Wang, et al. Pixel-perfect depth with semantics-prompted diffusion transformers. *arXiv preprint arXiv:2510.07316*, 2025. 3
- [110] Wei Xu, Charles James Wagner, Junjie Luo, and Qi Guo. Blurry-edges: Photon-limited depth estimation from defocused boundaries. In *Proceedings of the Computer Vision and Pattern Recognition Conference*, pages 432–441, 2025. 4
- [111] Fengting Yang, Xiaolei Huang, and Zihan Zhou. Deep depth from focus with differential focus volume. In *Proceedings of the IEEE/CVF conference on computer vision and pattern recognition*, pages 12642–12651, 2022. 2
- [112] Lihe Yang, Bingyi Kang, Zilong Huang, Xiaogang Xu, Jiashi Feng, and Hengshuang Zhao. Depth anything: Unleashing the power of large-scale unlabeled data. In *Proceedings of the IEEE/CVF conference on computer vision and pattern recognition*, pages 10371–10381, 2024. 3
- [113] Lihe Yang, Bingyi Kang, Zilong Huang, Zhen Zhao, Xiaogang Xu, Jiashi Feng, and Hengshuang Zhao. Depth anything v2. *Advances in Neural Information Processing Systems*, 37:21875–21911, 2024. 2, 3, 5, 6, 7, 8, 11, 12
- [114] Yang Yang, Haiting Lin, Zhan Yu, Sylvain Paris, and Jingyi Yu. Virtual dslr: High quality dynamic depth-of-field synthesis on mobile platforms. *Electronic Imaging*, 28:1–9, 2016. 3, 1, 2
- [115] Yang Yang, Siming Zheng, Jinwei Chen, Boxi Wu, Xiaofei He, Deng Cai, Bo Li, and Peng-Tao Jiang. Any-to-bokeh: One-step video bokeh via multi-plane image guided diffusion. *arXiv preprint arXiv:2505.21593*, 2025. 3
- [116] Hu Ye, Jun Zhang, Sibio Liu, Xiao Han, and Wei Yang. Ip-adapt: Text compatible image prompt adapter for text-to-image diffusion models. *arXiv preprint arXiv:2308.06721*, 2023. 4
- [117] Wei Yin, Chi Zhang, Hao Chen, Zhipeng Cai, Gang Yu, Kaixuan Wang, Xiaozhi Chen, and Chunhua Shen. Metric3d: Towards zero-shot metric 3d prediction from a single image. In *Proceedings of the IEEE/CVF international conference on computer vision*, pages 9043–9053, 2023. 3
- [118] Weihao Yuan, Xiaodong Gu, Zuozhuo Dai, Siyu Zhu, and Ping Tan. New crfs: Neural window fully-connected crfs for monocular depth estimation. *arXiv preprint arXiv:2203.01502*, 2022. 3
- [119] Yu Yuan, Xijun Wang, Yichen Sheng, Prateek Chennuri, Xingguang Zhang, and Stanley Chan. Generative photography: Scene-consistent camera control for realistic text-to-image synthesis. In *Proceedings of the Computer Vision and Pattern Recognition Conference*, pages 7920–7930, 2025. 7
- [120] Richard Zhang, Phillip Isola, Alexei A Efros, Eli Shechtman, and Oliver Wang. The unreasonable effectiveness of deep features as a perceptual metric. In *Proceedings of the IEEE conference on computer vision and pattern recognition*, pages 586–595, 2018. 6, 7
- [121] Xuaner Zhang, Kevin Matzen, Vivien Nguyen, Dillon Yao, You Zhang, and Ren Ng. Synthetic defocus and look-ahead autofocus for casual videography. *arXiv preprint arXiv:1905.06326*, 2019. 4
- [122] Peng Zheng, Dehong Gao, Deng-Ping Fan, Li Liu, Jorma Laaksonen, Wanli Ouyang, and Nicu Sebe. Bilateral reference for high-resolution dichotomous image segmentation. *arXiv preprint arXiv:2401.03407*, 2024. 2
- [123] Changyin Zhou, Stephen Lin, and Shree Nayar. Coded aperture pairs for depth from defocus. In *2009 IEEE 12th international conference on computer vision*, pages 325–332. IEEE, 2009. 5
- [124] Chengxuan Zhu, Qingnan Fan, Qi Zhang, Jinwei Chen, Huaqi Zhang, Chao Xu, and Boxin Shi. Bokehdiff: Neural lens blur with one-step diffusion. *arXiv preprint arXiv:2507.18060*, 2025. 2, 3, 6, 7, 8, 4, 5
- [125] Djemel Ziou and Francois Deschenes. Depth from defocus estimation in spatial domain. *Computer vision and image understanding*, 81(2):143–165, 2001. 5

BokehDepth: Enhancing Monocular Depth Estimation through Bokeh Generation

Supplementary Material

7. Stage-1 Background Details

7.1. FLUX-Kontext

FLUX-Kontext is a rectified flow transformer that unifies text-to-image (T2I) synthesis and instruction guided image editing in a single model [4]. Earlier systems such as SDXL [75, 83] or PixArt [13, 14] typically keep generation and editing in separate networks or attach task specific adapters to a base T2I model. In contrast, FLUX-Kontext uses one backbone for both tasks. The model operates in the latent space of a learned autoencoder [4, 83]: an input RGB image is encoded into a spatial latent grid, and all generation and editing is performed in that latent space before decoding back to pixels [75].

Instead of classical denoising diffusion, which learns to reverse a long noise corruption process through many discrete denoising steps [33, 75, 83, 92], FLUX-Kontext follows the flow-matching formulation [4, 21, 56]. Let $x_0 \sim q(x_0)$ be a clean latent sample from the data distribution and let $\varepsilon \sim \mathcal{N}(0, \mathbf{I})$ be Gaussian noise. We define a straight interpolation path between data and noise

$$x_t = (1 - t)x_0 + t\varepsilon, \quad t \in [0, 1], \quad (10)$$

$$\frac{dx_t}{dt} = v_\theta(x_t, t, c), \quad (11)$$

where v_θ is a time dependent velocity field predicted by a transformer under conditioning c . The model learns a velocity field that transports noise to data along this nearly linear path [21, 56]. Because x_t is a convex combination of x_0 and ε , the ideal instantaneous velocity is $(\varepsilon - x_0)$, which is constant in t . The training objective is

$$\min_{\theta} \mathbb{E}_{t, x_0, \varepsilon, c} \|\varepsilon - x_0 - v_\theta(x_t, t, c)\|_2^2. \quad (12)$$

At inference time, sampling integrates the learned ODE from $t = 1$ (noise) to $t = 0$ (clean latent) using only a few solver steps [4, 21, 56]. This yields fast image generation while preserving structural sharpness, readable text, and consistent identity.

For conditional generation and editing, FLUX-Kontext learns the conditional distribution $p(x_0 | y, c)$, where y is an optional visual reference such as a style or identity exemplar and c is a natural language instruction [4]. The current editable canvas x_0 , all reference images y , and the instruction c are encoded into tokens and concatenated into a single multimodal sequence processed by a large rectified-flow transformer related to the Multimodal Diffusion Transformer (MMDiT) that was introduced for high resolution

text to image synthesis under rectified flow training [4, 21]. Rotary Position Embedding (RoPE) [94] is generalized to three coordinates (t, h, w) , where (h, w) are spatial indices and t marks the source stream such as the editable canvas, each visual reference, or the text instruction. This positional encoding allows the transformer to attend across all sources in one pass while preserving both spatial layout and source identity [4]. A single backbone can therefore support pure generation, style transfer, identity preserving editing and iterative refinement in context across multiple user turns [4].

Editing in FLUX-Kontext is formulated as conditional generation rather than masked inpainting [4], which will be discussed in detail in Section 3.3. The model receives the editable canvas together with optional visual references and the text instruction and aligns them in latent space using scaled dot product attention [99]. Let Q , K , and V denote the query, key and value projections of the concatenated tokens. Attention is computed as

$$\text{Attention}(Q, K, V) = \text{Softmax}\left(\frac{QK^\top}{\sqrt{d}}\right)V. \quad (13)$$

During sampling, a rectified flow solver integrates the transformer’s learned velocity field to update the latent canvas under the fused conditioning signals, enabling precise edits, coherent global restyling, and stable subject identity across successive user-guided refinements [4, 21, 56].

7.2. Thin Lens Bokeh & Synthetic Bokeh Rendering

When a camera images a three dimensional scene onto a two dimensional sensor, only points at one specific focus distance appear perfectly sharp. Points in front of or behind that distance form small blurred disks on the sensor. These disks are known as circles of confusion (CoC) and they give rise to the familiar out of focus bokeh pattern in photography [46, 65, 89, 100, 114]. Under the thin lens model, the diameter d of the CoC depends on the lens geometry and the scene depth [46]. For a lens of focal length f and aperture N (that is, f number $N = f/A$ with entrance pupil diameter A), focused at distance S_1 while observing a subject at distance S_2 , the blur diameter is

$$d = \frac{f^2}{N(S_1 - f)} \frac{|S_2 - S_1|}{S_2}, \quad (14)$$

where S_1 is often called the focus distance and S_2 is the subject distance. Larger focal length f , wider aperture (smaller N), and greater separation between S_1 and S_2 all increase d ,

which produces stronger background blur and a more pronounced bokeh appearance [46, 100, 114].

Classical synthetic defocus methods approximate this physical effect by spreading, or splatting, each pixel over a disk whose radius matches its local blur size [64, 114]. Given per pixel disparity, the blur radius r can be written as

$$r = K \cdot \Delta\text{disp}, \quad \Delta\text{disp} = \left| \frac{1}{S_1} - \frac{1}{S_2} \right|, \quad (15)$$

where K is a camera-dependent scale that absorbs intrinsic parameters such as focal length and aperture [100, 114]. Pixels near the current focus distance S_1 receive a small blur radius and stay sharp, while pixels far from S_1 receive a large radius and become strongly blurred [64, 114].

This splatting model produces convincing shallow depth of field in regions that are smooth in depth, but it often fails near strong occlusion boundaries. At such boundaries, foreground colors can leak into the blurred background or background colors can wash across the foreground edge, which creates unnatural halos or color bleeding artifacts [65, 100]. Modern bokeh renderers address this limitation by making the process explicitly aware of occlusion and layering. One line of work uses neural refinement modules to inpaint or correct contaminated regions after classical splatting [65]. Another line decomposes the scene into ordered depth layers or multiplane images and composites them from back to front with explicit handling of partial occlusion. This layered or occlusion aware rendering strategy suppresses color bleeding at depth discontinuities and yields more realistic subject boundaries and foreground isolation [65, 89].

8. Stage-1 Dataset & Unified Training Details

8.1. T2I Dataset Details

We build on the hybrid dataset construction strategy introduced in Bokeh Diffusion [25] and adapt it to our T2I training setting. The first branch is a curated in-the-wild subset of roughly fifteen thousand Flickr-style photographs with permissive licenses. For each image, we record EXIF metadata capturing focal length and aperture, estimate dense metric depth using DepthPro [8], extract a high-resolution foreground mask [122], and obtain descriptive captions from large vision-language models. We remove samples with unreliable EXIF metadata, degenerate depth, or trivial foreground regions. About ten percent of the images are nearly all-in-focus and serve as sharp anchors.

The second branch is a synthetic augmentation subset. For each nearly all-in-focus anchor we render bokeh using a physically motivated defocus renderer such as BokehMe [65]. We estimate per-pixel disparity, sample a blur strength, and construct contrastive pairs that differ only in depth of field. These pairs teach the model that the same scene layout can appear either sharp or softly blurred, which is essential for controllable editing [25].

To train with a single conditioning signal, we express both real and rendered blur using a common scalar parameter K . Starting from the thin-lens model, the circle-of-confusion diameter for a point at subject distance S_2 when focusing at S_1 with focal length f and aperture N is

$$d = \frac{f^2}{N(S_1 - f)} \frac{|S_2 - S_1|}{S_2}. \quad (16)$$

Rewriting d in terms of the disparity difference $\Delta\text{disp} = \left| \frac{1}{S_1} - \frac{1}{S_2} \right|$ gives a radius proportional to Δdisp ,

$$K \approx \frac{f^2 S_1}{2N(S_1 - f)} \times \text{pixel_ratio}, \quad (17)$$

where `pixel_ratio` accounts for sensor pitch and target resolution. We compute S_1 from the median depth of the salient foreground region because EXIF metadata seldom records focus distance, and we discard scenes with unstable inferred S_1 . This conversion assigns each real photograph a physically grounded K consistent with the synthetic rendering parameter used by BokehMe, allowing real and synthetic samples to be mixed within a single training batch [25, 65].

Finally, we explain why we rely on this hybrid recipe instead of only using multi-aperture collections such as DPDD [1]. DPDD provides around five hundred controlled DSLR scenes with paired blurred and all-in-focus captures. These scenes are mostly static tabletop or indoor arrangements and rarely contain people in motion or crowded outdoor environments, which limits coverage. Our in-the-wild branch covers dynamic subjects, complex human-centric shots, and diverse compositions, while the synthetic branch supplies precise focus and defocus supervision with continuous aperture control. Together they yield a dataset that supports physically grounded bokeh control and identity-preserving editing in our model [25].

8.2. Scene-consistent T2I Bokeh Generation

To ensure that the T2I synthesized bokeh stack maintains consistent scene structure and subject identity across varying defocus levels, we adopt the generation pipeline proposed in Bokeh Diffusion [25]. This framework employs a grounded self-attention mechanism to anchor the spatial layout to a pivot image and utilizes a color transfer step to harmonize illumination statistics. Although our inference stage targets image-to-image editing, we implement part of the training process as a text-to-image task. This strategy allows us to leverage extensive unpaired in-the-wild photography to learn robust optical properties rather than relying solely on limited paired supervision.

8.3. Bokeh Strength Alignment Across I2I datasets

Stage-1 I2I training uses a single scalar bokeh strength K to control the blur magnitude per unit-disparity, matching the



Figure 6. Illustration of some samples from the SYSTHEBOKEH300 validation set.

thin-lens formulation in Equation (17). To mix real photographs, captured triplets, and synthetic renders in a single model, we convert all image-to-image bokeh datasets into a unified JSONL schema. Each row stores the input all-in-focus image, the target bokeh image, an optional depth map, and a `camera_anns` dictionary that contains the aperture N , focal length f_{mm} , 35 mm-equivalent focal length $f_{35\text{mm}}$, sensor width, focus distance S_1 , and a calibrated bokeh strength field `dof-cond`. A crop-corrected variant `dof-cond-crop` records the same quantity normalized to a full-frame field of view. All K values are obtained by calling a single thin-lens utility `calc_dof_cond`, which implements Equation (17) and returns the expected circle-of-confusion diameter in pixels for a given configuration, then normalizes it to a reference width of 512.

DPDD indoor Canon CR2. The DPDD indoor split contains Canon RAW image pairs captured with different f -numbers under fixed scene geometry. Our conversion script calls `exiftool` on all `.CR2` files and parses `CreateDate`, `FNumber`, `FocalLength`, `ApproximateFocusDistance`, `FocusDistanceUpper`, `FocusDistanceLower`, and the focal-plane resolution and image dimension fields. For each exposure, we estimate the focus distance S_1 in meters by using `ApproximateFocusDistance` when present and otherwise averaging `FocusDistanceUpper` and `FocusDistanceLower`. We sort images by time, form candidate pairs within a short temporal window that match

in focal length and focus distance, and designate within each group the smallest f -number as the bokeh target and the largest f -number as the all-in-focus source.

For every selected bokeh shot we estimate the sensor width in millimeters in a multi-step fashion. When focal-plane resolution and resolution units are available, we convert pixels to millimeters using the reported pitch. If this fails, we fall back to inverting f_{mm} and $f_{35\text{mm}}$ through `calc_sensor_width`, and finally use camera-model heuristics for common Canon full-frame and APS-C bodies based on the EXIF `Model` string and image resolution. With N , f_{mm} , $f_{35\text{mm}}$, S_1 , and the target image size (W, H) in hand, we call `calc_dof_cond` to obtain a physically grounded blur slope K at the native resolution. This value is rescaled to a reference width of 512 by multiplying with $512/W$ and stored in `dof-cond`. When both f_{mm} and $f_{35\text{mm}}$ are known, we also compute the crop factor and divide `dof-cond` by this factor to obtain a full-frame aligned value `dof-cond-crop`. Finally, a relaxed depth-of-field test based on the near and far bounds in Equation (17) and a sensor-size-dependent circle-of-confusion estimate marks each row with a boolean `foreground_clear` flag, which indicates whether a near-foreground plane remains inside the in-focus region.

Aperture-Dataset. The Aperture-Dataset contains captured triplets with a fixed scene and focus setting and three apertures: a small aperture ($f/22$) that is close to pinhole imaging and two bokeh views ($f/8$ and $f/2$) that share

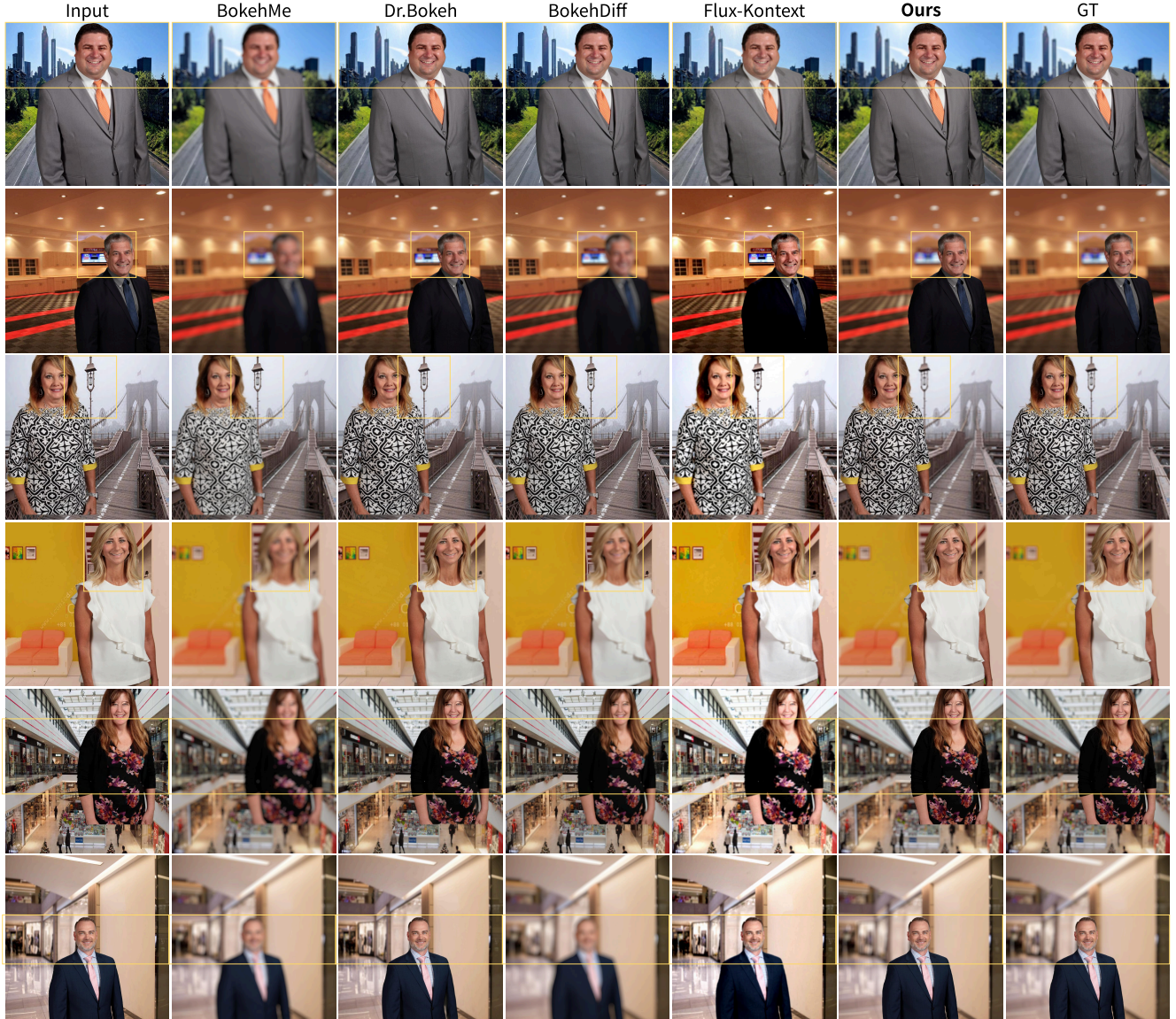


Figure 7. Qualitative comparisons for SystheBokeh300 (synthetic) between our Stage-1 model, BokehMe [65], Dr. Bokeh [89], BokehDiff [124], FLUX-Kontext [4], and the ground truth. Our method more reliably preserves in-focus subjects while producing background blur that increases monotonically with depth. At depth discontinuities, it substantially reduces edge halos and color bleeding. Overall, the rendered bokeh is visually closer to the ground truth.

a common metric depth map. We convert this dataset by treating the $f/22$ image as the input all-in-focus source and the $f/8$ or $f/2$ image as the target bokeh output. Since focus distance is not stored in EXIF, we estimate S_1 from the depth map. For each scene, we resize the depth map to match the $f/22$ view, compute image gradients on the sharp RGB image, and form a gradient-weighted median over depth values along high-frequency edges. This yields a robust estimate of the physical focus distance that concentrates on visually salient structures.

Camera parameters for Aperture-Dataset are set through

explicit defaults. We assume a Canon EOS body with a 50 mm lens, full-frame sensor width of 36 mm, and crop factor 1.0, while allowing these values to be overridden by command-line arguments. Given $N_{\text{bokeh}} \in \{8.0, 2.0\}$, f_{mm} , $f_{35\text{mm}}$, the recovered S_1 , and the target image size, we compute K with `calc_dof_cond` and again normalize it to a width of 512. The resulting values are stored as `dof_cond` and `dof_cond_crop` in `camera_anns` for each bokeh level. The same relaxed depth-of-field criterion as in DPDD is applied to label `foreground_clear`. Although both bokeh targets share the same all-in-focus source and



Figure 8. Qualitative comparisons for EBB! Val200 (real) [38, 67] between our Stage-1 model, BokehMe [65], Dr. Bokeh [89], BokehDiff [124], FLUX-Kontext [4], and the ground truth. Our method more reliably preserves in-focus subjects while producing background blur that increases monotonically with depth. At depth discontinuities, it substantially reduces edge halos and color bleeding. Overall, the rendered bokeh is visually closer to the ground truth.

focus distance, their different f -numbers produce distinct K values, which lets the model learn how bokeh strength changes as the physical aperture opens.

BLB synthetic renders. The BLB dataset provides fully rendered defocus stacks with known intrinsics and focus distances. Each scene directory contains a sharp RGB image, a disparity map, a set of bokeh renders indexed by focus and aperture, and an `info.json` file listing the physical parameters: focus distances, f -stop values, focal length, sensor width, and rendered resolution. Our pipeline converts `disparity.jpg` into an approximate metric depth map (`.npz`), treats `focal_length` and `sensor_width` as ground truth, converts them to millimeters, and computes a 35 mm-equivalent focal length and crop factor.

The renderer supplies a normalized f -stop rather than a conventional f -number. We map each f -stop to a continuous f -number between roughly $f/1.4$ and $f/16$ using logarithmic interpolation over a standard aperture series, and use this value as N in Equation (17). For each valid focus–aperture pair with an available bokeh render, we compute K at two resolutions using the same thin-lens utility. We call `calc_dof_cond` at the native BLB resolution ($W_{\text{orig}}, H_{\text{orig}}$) for the FLUX branch. Outputs are clipped to $[0, 30]$ for stability and stored as `dof_cond` (native) and `dof_cond_crop` (512-normalized). We also compute a scalar `disp_focus` capturing the scene’s relative focus

depth and combine it with an analytic depth-of-field test, based on the near and far bounds from Equation (17), to produce a permissive `foreground_clear` label.

Discussion. Across DPDD, Aperture-Dataset, and BLB, the concrete estimation route for S_1 , sensor size, and aperture differs, yet all three pipelines reduce to the same thin-lens function `calc_dof_cond` and the same reference-width and crop-factor conventions. As a result, every I2I training pair carries a physically grounded and numerically comparable bokeh strength K in its `camera_anns`. This alignment lets Stage-1 share a single bokeh-attention branch across real DSLR photographs, captured depth-assisted triplets, and synthetic renders, while interpreting the requested bokeh strength on a consistent metric scale.

9. Mathematical Proofs

Proposition 1 (Depth-from-Bokeh Sweep under Calibrated Bokeh Control). *For a static scene observed by a thin-lens camera with fixed pose and focus distance, we record a bokeh stack by sweeping only the calibrated bokeh strength K . At every pixel, the measured bokeh radius is exactly proportional to that pixel’s inverse-depth offset from the focal plane. The slope of this proportionality, obtained by regressing radius on K across the stack, is an unbiased and consistent estimate of that offset and yields the pixel’s met-*

ric depth up to the usual front/behind-focus sign.

Proof. Consider a thin-lens camera of focal length f , held at a fixed viewpoint. Let the lens be focused at object distance $S_1 > f$. For any pixel location x in the image plane, let $S_2(x)$ denote the distance from the lens to the 3D scene point that projects to x . We define the per-pixel inverse-depth offset from the focal plane,

$$\Delta(x) := \left| \frac{1}{S_1} - \frac{1}{S_2(x)} \right|. \quad (18)$$

We now describe the bokeh sweep acquisition. We capture m images $\{I_{K_i}\}_{i=1}^m$ of the same static scene from the same pose and with the same focus distance S_1 , while sweeping only a calibrated bokeh strength K_i for each frame i . Concretely, frame i is taken with a (aperture) pupil diameter A_i and f -number $N_i = f/A_i$, and changing A_i changes K_i but leaves all other camera parameters, including the camera pose and the focus distance S_1 , fixed. At each setting i , the observed image around pixel x is modeled (locally, under a spatially shift-invariant defocus approximation) as a convolution of an all-in-focus radiance image J with an isotropic pillbox PSF of radius $r_i(x)$, plus zero-mean noise $\eta_i(x)$:

$$I_{K_i}(x) = (h_{r_i(x)} * J)(x) + \eta_i(x), \quad (19)$$

where $h_{r_i(x)}$ is a disk PSF of radius $r_i(x)$ in output pixels and $\mathbb{E}[\eta_i(x)] = 0$.

We next express $r_i(x)$ in terms of scene geometry and aperture. Under the paraxial thin-lens model, the circle of confusion (CoC) produced on the sensor by a scene point at distance $S_2(x)$, when the lens is focused at S_1 , has diameter (in physical sensor-length units)

$$d_i(x) = \frac{|S_2(x) - S_1|}{S_2(x)} \frac{f^2}{N_i(S_1 - f)}. \quad (20)$$

Equation (20) follows directly from similar triangles and the thin-lens relation, and is exact in the paraxial regime for a thin lens with a circular aperture of diameter $A_i = f/N_i$.

We rewrite the geometric factor in (20) using inverse distances. First note that

$$\left| \frac{1}{S_1} - \frac{1}{S_2(x)} \right| = \left| \frac{S_2(x) - S_1}{S_1 S_2(x)} \right| = \frac{|S_2(x) - S_1|}{S_1 S_2(x)}. \quad (21)$$

Multiplying both sides of (21) by S_1 gives

$$S_1 \left| \frac{1}{S_1} - \frac{1}{S_2(x)} \right| = \frac{|S_2(x) - S_1|}{S_2(x)}. \quad (22)$$

Substituting (22) into (20) yields

$$d_i(x) = \frac{f^2}{N_i(S_1 - f)} S_1 \left| \frac{1}{S_1} - \frac{1}{S_2(x)} \right| = \frac{f^2 S_1}{N_i(S_1 - f)} \Delta(x), \quad (23)$$

where $\Delta(x)$ is the inverse-depth offset defined in (18).

The pillbox PSF $h_{r_i(x)}$ is parameterized in terms of its radius $r_i(x)$ in *output pixels* rather than physical sensor units. Let `pixel_ratio` > 0 denote the known conversion factor from sensor-length units to output pixels, and recall that $r_i(x)$ is half the CoC diameter measured in pixels. Then

$$r_i(x) = \frac{1}{2} d_i(x) \text{pixel_ratio} = \frac{1}{2} \left[\frac{f^2 S_1}{N_i(S_1 - f)} \Delta(x) \right] \text{pixel_ratio}. \quad (24)$$

All terms in brackets in (24) that depend on the aperture index i but not on scene depth at x can be grouped into a known scalar $K_i > 0$, which we call the calibrated defocus gain for aperture i :

$$K_i := \frac{1}{2} \frac{f^2 S_1}{N_i(S_1 - f)} \text{pixel_ratio}. \quad (25)$$

This K_i is exactly the per-frame calibrated bokeh strength mentioned in Proposition 1: it folds known camera quantities (f , N_i), the fixed focus distance S_1 , and the pixel scaling factor into a single scalar. By construction, K_i varies only because we deliberately change the aperture for frame i , while the scene geometry and S_1 stay fixed.

With the calibrated defocus gain for aperture i , (24) yields the exact per-pixel linear defocus law

$$r_i(x) = K_i \Delta(x) \quad \text{for each } i = 1, \dots, m. \quad (26)$$

Equation (26) implies that for a fixed pixel x , all $(K_i, r_i(x))$ pairs fall on a single origin-passing line with slope $\Delta(x)$.

In practice, the "measured bokeh radius" referred to in Proposition 1 is obtained from each captured frame rather than taken as the ideal geometric radius $r_i(x)$ itself. We therefore do not observe $r_i(x)$ directly; instead we estimate it from the captured image I_{K_i} , e.g. by fitting a pillbox PSF radius. Let $\hat{r}_i(x)$ denote such a per-frame estimate, and assume it is unbiased with finite variance:

$$\mathbb{E}[\hat{r}_i(x)] = r_i(x), \quad \text{Var}[\hat{r}_i(x)] < \infty. \quad (27)$$

We now form the ordinary least-squares (OLS) slope through the origin that regresses $\hat{r}_i(x)$ against K_i :

$$\hat{\Delta}(x) := \frac{\sum_{i=1}^m K_i \hat{r}_i(x)}{\sum_{i=1}^m K_i^2}. \quad (28)$$

To show that $\hat{\Delta}(x)$ is unbiased for $\Delta(x)$, we first substitute (26) into (27), which implies

$$\mathbb{E}[\hat{r}_i(x)] = r_i(x) = K_i \Delta(x). \quad (29)$$

Taking expectation of (28) and applying (29) termwise in

the numerator,

$$\mathbb{E}[\widehat{\Delta}(x)] = \mathbb{E}\left[\frac{\sum_{i=1}^m K_i \widehat{r}_i(x)}{\sum_{i=1}^m K_i^2}\right] = \frac{\sum_{i=1}^m K_i \mathbb{E}[\widehat{r}_i(x)]}{\sum_{i=1}^m K_i^2} \quad (30)$$

$$= \frac{\sum_{i=1}^m K_i (K_i \Delta(x))}{\sum_{i=1}^m K_i^2} = \frac{\Delta(x) \sum_{i=1}^m K_i^2}{\sum_{i=1}^m K_i^2} = \Delta(x). \quad (31)$$

Hence $\widehat{\Delta}(x)$ is an unbiased estimator of the inverse-depth offset $\Delta(x)$.

We now examine its variance. Assume that the random errors across different aperture settings are uncorrelated, i.e. $\widehat{r}_i(x)$ and $\widehat{r}_j(x)$ are independent for $i \neq j$, and that each $\widehat{r}_i(x)$ has finite variance. Then from (28),

$$\begin{aligned} \text{Var}[\widehat{\Delta}(x)] &= \text{Var}\left[\frac{\sum_{i=1}^m K_i \widehat{r}_i(x)}{\sum_{i=1}^m K_i^2}\right] \\ &= \frac{1}{\left(\sum_{i=1}^m K_i^2\right)^2} \sum_{i=1}^m K_i^2 \text{Var}[\widehat{r}_i(x)]. \end{aligned} \quad (32)$$

Because the denominator in (32) grows as $(\sum_{i=1}^m K_i^2)^2$, the variance decays on the order of $1/\sum_{i=1}^m K_i^2$. In particular, if $\sum_{i=1}^m K_i^2 \rightarrow \infty$ as $m \rightarrow \infty$, then $\text{Var}[\widehat{\Delta}(x)] \rightarrow 0$, so $\widehat{\Delta}(x)$ is consistent for $\Delta(x)$.

Finally, we recover metric depth. From (18), we have

$$\Delta(x) = \left| \frac{1}{S_1} - \frac{1}{S_2(x)} \right| \implies \frac{1}{S_2(x)} = \frac{1}{S_1} \pm \Delta(x). \quad (33)$$

The \pm corresponds to the front/back ambiguity of defocus: a point in front of the focal plane and a symmetric point behind it yield the same absolute offset $\Delta(x)$. Replacing $\Delta(x)$ by the unbiased, consistent estimator $\widehat{\Delta}(x)$ from (28) gives the per-pixel metric depth estimate

$$\frac{1}{S_2(x)} = \frac{1}{S_1} \pm \widehat{\Delta}(x), \quad S_2(x) = \left(\frac{1}{S_1} \pm \widehat{\Delta}(x) \right)^{-1}. \quad (34)$$

Taken together, Equations (26), (31), and (34) show that a calibrated sweep of $\{K_i\}_{i=1}^m$ induces a per-pixel linear bokeh-versus-inverse-depth relationship $r_i(x) = K_i \Delta(x)$ whose slope is precisely the inverse-depth offset $\Delta(x)$, and that, under the finite-variance and independence assumptions stated above, the OLS slope $\widehat{\Delta}(x)$ in (28) is an unbiased and consistent estimator of $\Delta(x)$ as m increases (since $\text{Var}[\widehat{\Delta}(x)] \rightarrow 0$ when $\sum_i K_i^2 \rightarrow \infty$); substituting this estimator into (34) then yields a per-pixel metric depth estimate, subject only to the standard in-front / behind-focus sign ambiguity of defocus. \square

10. Definition of Evaluation Metrics

We evaluate both stages of our pipeline using established metrics in image synthesis and monocular depth estimation. Below we summarize the definitions adopted in this work.

Stage-1: Bokeh synthesis quality. Given a reference bokeh image B and a synthesized bokeh image \hat{B} of size $H \times W$, we first measure distortion with peak signal-to-noise ratio (PSNR) and structural similarity (SSIM). PSNR is defined as

$$\text{PSNR}(B, \hat{B}) = 10 \log_{10} \left(\frac{L^2}{\text{MSE}(B, \hat{B})} \right), \quad (35)$$

where L is the maximum possible pixel value and

$$\text{MSE}(B, \hat{B}) = \frac{1}{HW} \sum_p \|B(p) - \hat{B}(p)\|_2^2 \quad (36)$$

is the mean squared error over all pixels p . SSIM measures local luminance, contrast and structural consistency between B and \hat{B} . Following [105], we compute the SSIM index over sliding windows as

$$\text{SSIM}(B, \hat{B}) = \frac{(2\mu_B \mu_{\hat{B}} + C_1) (2\sigma_{B\hat{B}} + C_2)}{(\mu_B^2 + \mu_{\hat{B}}^2 + C_1) (\sigma_B^2 + \sigma_{\hat{B}}^2 + C_2)}, \quad (37)$$

where μ_B and $\mu_{\hat{B}}$ are local means, σ_B^2 and $\sigma_{\hat{B}}^2$ are local variances, $\sigma_{B\hat{B}}$ is the local covariance, and C_1, C_2 are small constants that stabilize the ratio. Higher PSNR and SSIM indicate better bokeh reconstruction quality.

To better capture perceptual fidelity, we also report LPIPS [120] and DISTS [16]. LPIPS compares deep features extracted by a pretrained network and averages the channel-wise distance over spatial locations

$$\text{LPIPS}(B, \hat{B}) = \sum_{\ell} w_{\ell} \frac{1}{|\Omega_{\ell}|} \sum_{p \in \Omega_{\ell}} \left\| \phi_{\ell}(B)_p - \phi_{\ell}(\hat{B})_p \right\|_2^2, \quad (38)$$

where $\phi_{\ell}(\cdot)$ denotes features at layer ℓ , Ω_{ℓ} is the corresponding spatial grid, and w_{ℓ} are learned scalar weights. DISTS computes a weighted combination of structure and texture similarity in deep feature space

$$\text{DISTS}(B, \hat{B}) = \sum_{\ell} [\alpha_{\ell}(1 - S_{\ell}(B, \hat{B})) + \beta_{\ell}(1 - T_{\ell}(B, \hat{B}))], \quad (39)$$

where S_{ℓ} measures structural similarity between normalized features, T_{ℓ} measures texture similarity through feature magnitudes, and $\alpha_{\ell}, \beta_{\ell}$ are learned nonnegative weights. Lower LPIPS and DISTS indicate that synthesized bokeh images are closer to the reference in a feature space that correlates with human perception. All image quality metrics are computed on linear RGB images, cropped to the valid field of view of each dataset.

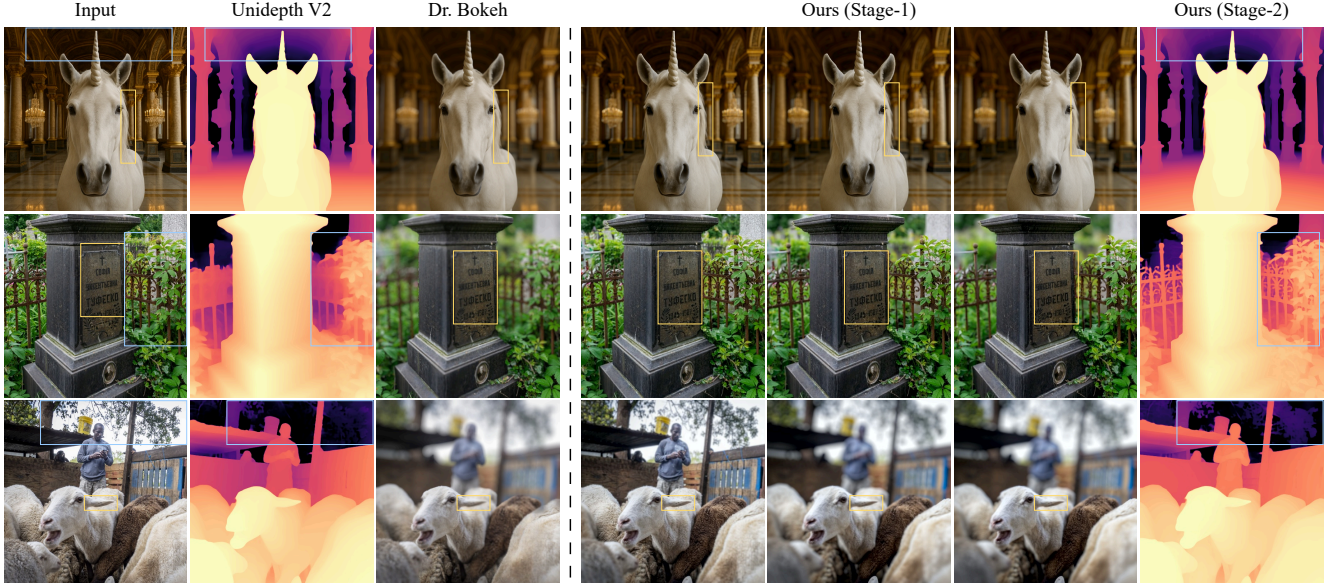


Figure 9. More qualitative results of *BokehDepth*. *Left*: conventional pipelines predict depth from a single sharp image and render bokeh from the noisy depth map. *Right*: our two-stage framework, where Stage-1 generates a calibrated bokeh stack with multiple bokeh strengths from a single image and Stage-2 built on UniDepthV2 [74] fuses defocus cues to produce sharper and more reliable metric depth.

Stage-2: Metric depth estimation. For Stage-2, we evaluate predicted metric depth maps against ground-truth depth using standard monocular depth metrics. Let D be the predicted depth map and D^* the ground-truth depth, defined on the set of valid pixels \mathcal{V} . The absolute relative error (AbsRel) is defined as

$$\text{AbsRel} = \frac{1}{|\mathcal{V}|} \sum_{p \in \mathcal{V}} \frac{|D(p) - D^*(p)|}{D^*(p)}. \quad (40)$$

We treat lower AbsRel as better and report it as our main scalar error metric in tables and ablations.

We also report the common threshold accuracy δ_1 , which measures the fraction of pixels where the prediction is close to the ground truth up to a multiplicative factor

$$\delta_1 = \frac{1}{|\mathcal{V}|} \left| \left\{ p \in \mathcal{V} \mid \max \left(\frac{D(p)}{D^*(p)}, \frac{D^*(p)}{D(p)} \right) < 1.25 \right\} \right|. \quad (41)$$

Higher δ_1 indicates better agreement between predicted and true depths. For completeness, we also monitor squared relative error (SqRel), root mean squared error (RMSE), and RMSE in log space on the validation sets. Following standard depth-estimation benchmarks, SqRel for a prediction \hat{D} and ground-truth depth D over pixels Ω is defined as

$$\text{SqRel} = \frac{1}{|\Omega|} \sum_{p \in \Omega} \frac{(D_p - \hat{D}_p)^2}{D_p}, \quad (42)$$

and RMSE is defined as

$$\text{RMSE} = \sqrt{\frac{1}{|\Omega|} \sum_{p \in \Omega} (D_p - \hat{D}_p)^2}, \quad (43)$$

with RMSE_{\log} computed analogously in log space. We omit some of these metrics from the main tables when their trends are consistent with the primary ones. All depth metrics are computed in metric units on the valid depth range of each dataset without scale alignment, following the standard protocol used in recent monocular metric depth work.

11. Details of *SYSTHEBOKEH300* Dataset

SYSTHEBOKEH300, shown in Figure 6, is a synthetic benchmark that exposes fine-grained control over defocus strength and focal distance under fully known geometry. The dataset is built on a two-layer multi-plane image representation rendered with a ray-traced thin-lens model. For each scene we provide a sharp all-in-focus image, a floating point disparity map and multiple bokeh images rendered under different aperture and focus settings. All images are RGB at a resolution of 1024×1024 .

We construct each scene by compositing a foreground RGBA matte over a natural background photograph. Foreground assets are PNG images with transparency that capture objects with complex silhouettes such as people, plants and everyday items. The generator first crops the foreground to the tight alpha bounding box, then randomly rescales it so that the projected area occupies roughly

30%–80% of the final frame. The resized foreground is placed near the image center with a small random offset while we ensure that it remains fully inside the background canvas. Background images are resized to a slightly larger canvas than the final resolution to absorb boundary effects introduced by lens blur. After rendering we crop a central 1024×1024 window which defines a single all-in-focus reference image per foreground–background pair.

Depth in *SYSTHEBOKEH300* is defined in disparity space to match the thin-lens formulation used for camera calibration in our real-image datasets. For the background we sample a random planar disparity field

$$d_{\text{bg}}(x, y) = \frac{c}{1 - ax - by}, \quad (44)$$

where (a, b, c) are normalized so that d_{bg} remains within a bounded range over the image grid. The foreground is assigned a separate planar disparity band whose values lie closer to the camera than the background disparity within the alpha support, ensuring smooth disparity in both layers and a consistent occlusion order. We store the final per-pixel disparity map $d(x, y)$ for each scene as a single-channel `float32` array, providing ground-truth metric depth up to a global scale factor.

Given the layered scene representation we render defocus using a reverse ray-tracing module. For each scene the renderer takes as input the linear RGB foreground and background layers, their opacity masks and the corresponding disparity coefficients and simulates a thin lens with a finite aperture. We parameterize defocus by a dimensionless blur strength K and a normalized focus disparity $d_f \in [0, 1]$. The renderer uses K to scale the circle-of-confusion radius in disparity space as

$$\Delta d(x, y) = K \frac{d(x, y) - d_f}{s}, \quad (45)$$

with s a fixed defocus scale factor. The module integrates multiple rays per pixel to obtain a bokeh image in linear RGB, which is then converted back to display gamma with exponent $1/\gamma$ with $\gamma = 2.2$.

For each foreground–background combination we keep the geometry fixed and vary only the lens parameters. The generator samples K from a wide range that spans both subtle and strong blur, and restricts d_f to the foreground-focused regime so that synthesized views keep the main subject sharp while varying the background blur. In our default configuration we draw three values of K and one value of d_f , which yields three distinct bokeh renderings per scene while sharing a single all-in-focus image and disparity map. We also map each sampled K to an equivalent f -number in the range $[1.4, 22]$ in order to align the synthetic lens settings with typical DSLR cameras. The sampling policy is encoded in the metadata and matches the dis-

tribution of lens parameters used when training the editing model on real-camera datasets.

The final dataset is organized under four top-level directories: `aif` for all-in-focus inputs, `images` for bokeh renderings, `depth` for disparity maps and `metadata` for per-image JSON descriptors. Each bokeh image is stored as an 8-bit JPEG in `images` and has a corresponding JSON file in `metadata` that records its identifier, the shared all-in-focus and depth file paths, the sampled K and d_f , the equivalent f -number and basic renderer settings.

During evaluation *SYSTHEBOKEH300* provides photo-realistic yet fully controllable test cases in which we can measure both image reconstruction quality and depth-aware consistency across changes in aperture and focus under ground-truth geometry.

12. Ablation on Stage-1 Inference Steps



Figure 10. Qualitative results of the ablation on the number of Stage-1 inference steps. From left to right and top to bottom we show the ground-truth bokeh image, followed by *BokehDepth* results with 50, 20, 10, 5, and 1 inference step on the same scene.

To understand how the number of reverse diffusion steps in Stage-1 affects bokeh synthesis quality, we evaluate *BokehDepth* on the *SYSTHEBOKEH300* validation set under different numbers of inference steps. Table 5 reports standard distortion and perceptual metrics for 50, 10, 5, and 1 sampling steps.

Using 50 steps yields the best overall reconstruction quality, but the gap between 50 and 10 steps is modest in both PSNR and SSIM, and the perceptual metrics remain close. Comparing with the results in Figure 10, reducing the step count further to 5 or 1 leads to clear degradation across almost all metrics, which indicates insufficient convergence

Steps	PSNR \uparrow	SSIM \uparrow	LPIPS \downarrow	DISTS \downarrow
50	29.1215	0.9011	0.1385	0.0725
10	27.8744	0.8900	0.1444	0.0751
5	28.2572	0.8829	0.1584	0.0824
1	24.8304	0.8539	0.1671	0.0946

Table 5. Ablation on the number of Stage-1 inference steps on the SYSTHEBOKEH300 validation set.

of the diffusion sampler and more noticeable artifacts in the synthesized bokeh.

Considering the cost of generating a full bokeh stack for Stage-2, we adopt 10 diffusion steps for all Stage-1 bokeh stack generation. This configuration achieves a balanced trade off between fidelity and efficiency and keeps the training and evaluation pipeline computationally practical.

13. Additional Qualitative Results

We provide additional qualitative results for Stage-1 in Figure 7 and Figure 8, and for the full pipeline in Figure 9, Figure 11, and Figure 12.

14. Limitations and Future Work.

Although the two stage *BokehDepth* framework can generate controllable high quality bokeh and consistently improve monocular depth estimation, The current pipeline is still trained in a decoupled manner. The synthesized bokeh stack from the first stage is only used by the second stage, so the depth branch cannot provide geometric feedback to improve the generated blur. This limits how much implicit information can be shared between the two tasks. A natural next step is an end-to-end model built on an image editing backbone that takes a single sharp RGB image and jointly predicts a multi-level bokeh stack and the metric depth of the reference frame. In such a setup, depth errors can inform the realism of bokeh generation, and the bokeh stack can provide stronger depth cues to the depth branch.

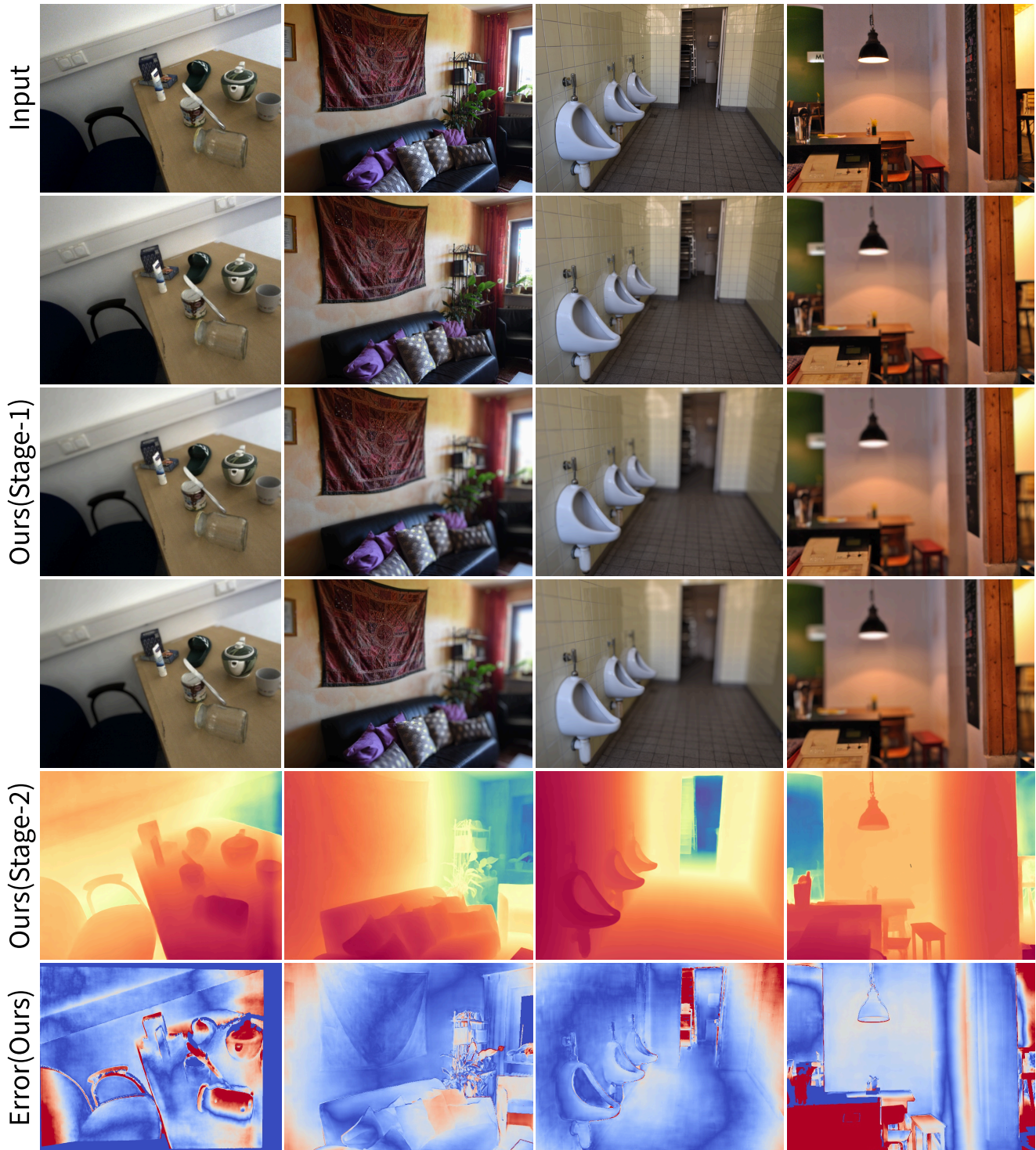


Figure 11. Qualitative results of *BokehDepth* using the Depth Anything V2 [113] backbone. From top to bottom: the input image, three representative frames from the Stage-1 bokeh stack, the Stage-2 depth prediction, and the error map of *BokehDepth*.

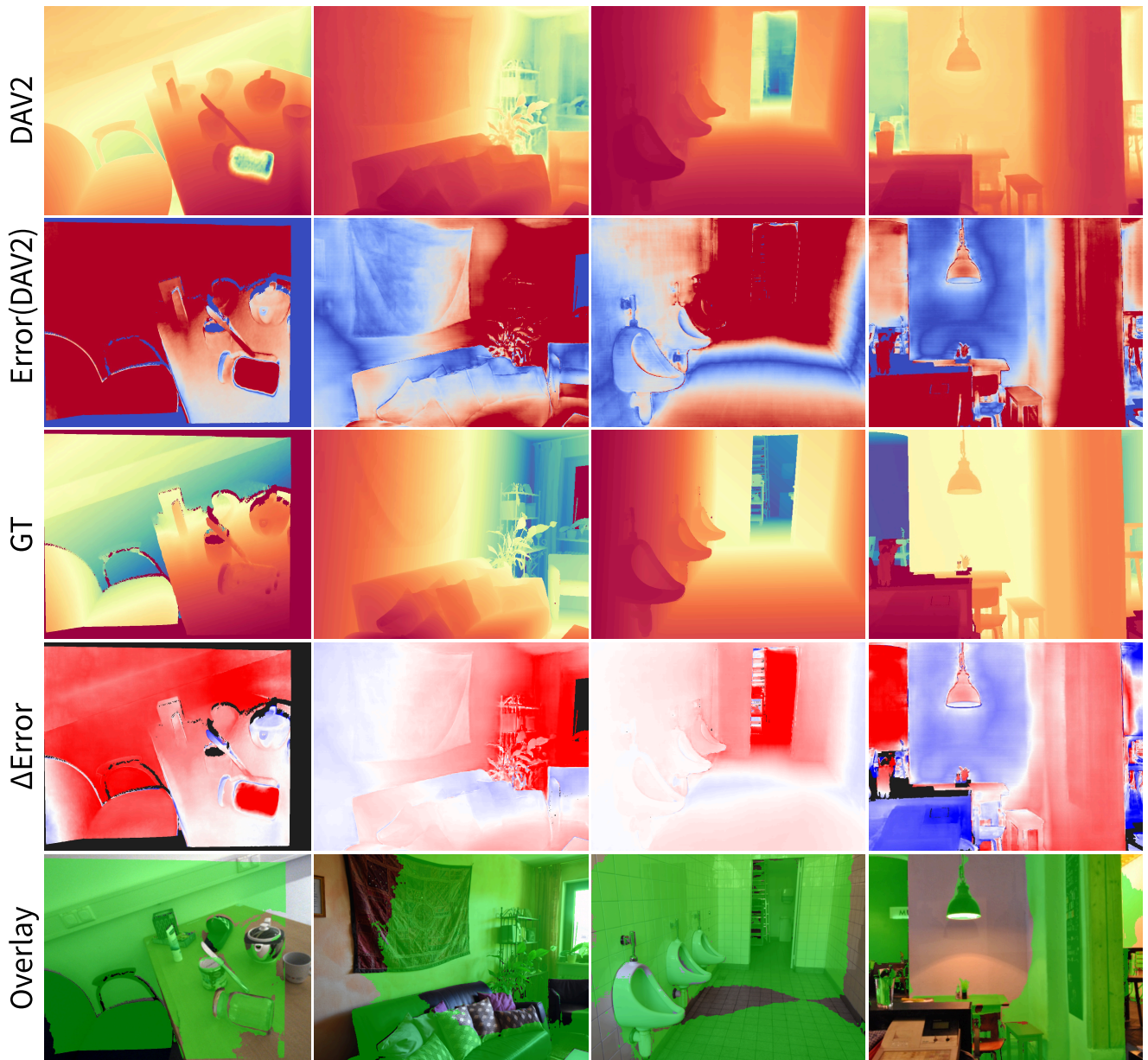


Figure 12. Qualitative results of *BokehDepth* using the Depth Anything V2 [113] backbone (continued from Figure 11). From top to bottom: the Depth Anything V2 prediction, the corresponding error map, the ground truth depth, the Δ Error map that reports the per-pixel reduction in absolute depth error of *BokehDepth* over the base model, and the RGB image overlaid with green regions that mark where our method produces notable improvements. *BokehDepth* lowers depth errors on fine structures, weakly-textured walls and distant background regions, offering more distinct layer separation and steadier metric depth across varied scenes.